LBL-113 c.1

RECEIVED
LAWRENCE
RADIATION LABORATORY

LIBRARY AND
DOCUMENTS SECTION

THEORETICAL AND EXPERIMENTAL STUDIES OF FLOW AND FRACTURE IN MONOCRYSTALLINE SILICON

Charles Falding St. John
(Ph. D. Thesis)

August 1971

AEC Contract No. W-7405-eng-48

For Reference

Not to be taken from this room

LBL-113 c.1

DISCLAIMER

This document was prepared as an account of work sponsored by the United States Government. While this document is believed to contain correct information, neither the United States Government nor any agency thereof, nor the Regents of the University of California, nor any of their employees, makes any warranty, express or implied, or assumes any legal responsibility for the accuracy, completeness, or usefulness of any information, apparatus, product, or process disclosed, or represents that its use would not infringe privately owned rights. Reference herein to any specific commercial product, process, or service by its trade name, trademark, manufacturer, or otherwise, does not necessarily constitute or imply its endorsement, recommendation, or favoring by the United States Government or any agency thereof, or the Regents of the University of California. The views and opinions of authors expressed herein do not necessarily state or reflect those of the United States Government or any agency thereof or the Regents of the University of California.

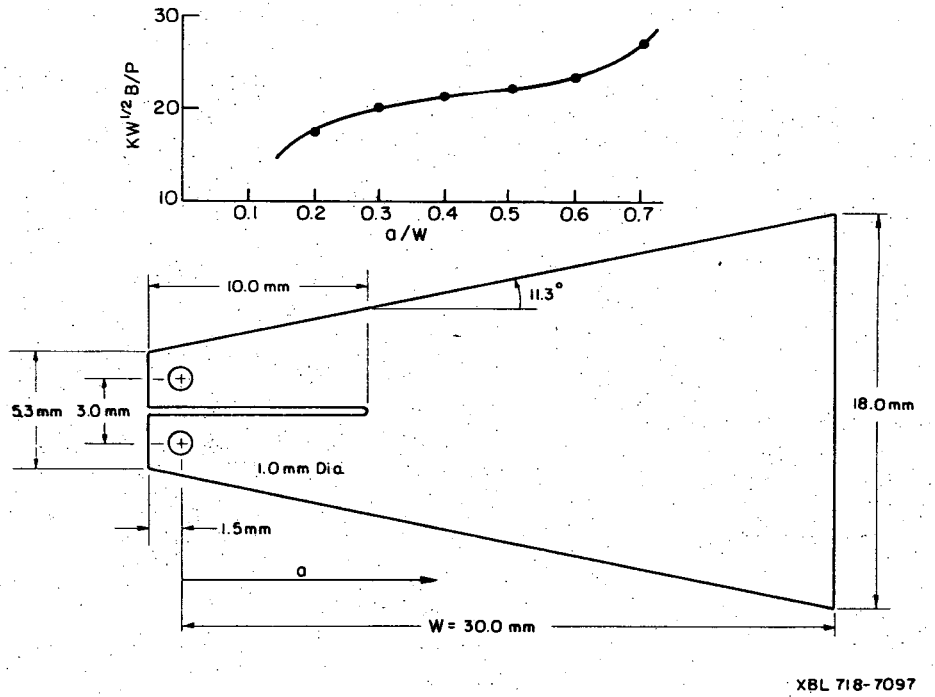
30
20
10
$KW^{1/2}B/P$
0.1
0.2
0.3
0.4
0.5
0.6
0.7
a/W
10.0 mm
11.3°
5.3mm
3.0 mm
1.0mm Dia.
1.5mm
a
W = 30.0 mm
18.0mm
XBL 718-7097

Fig. 1

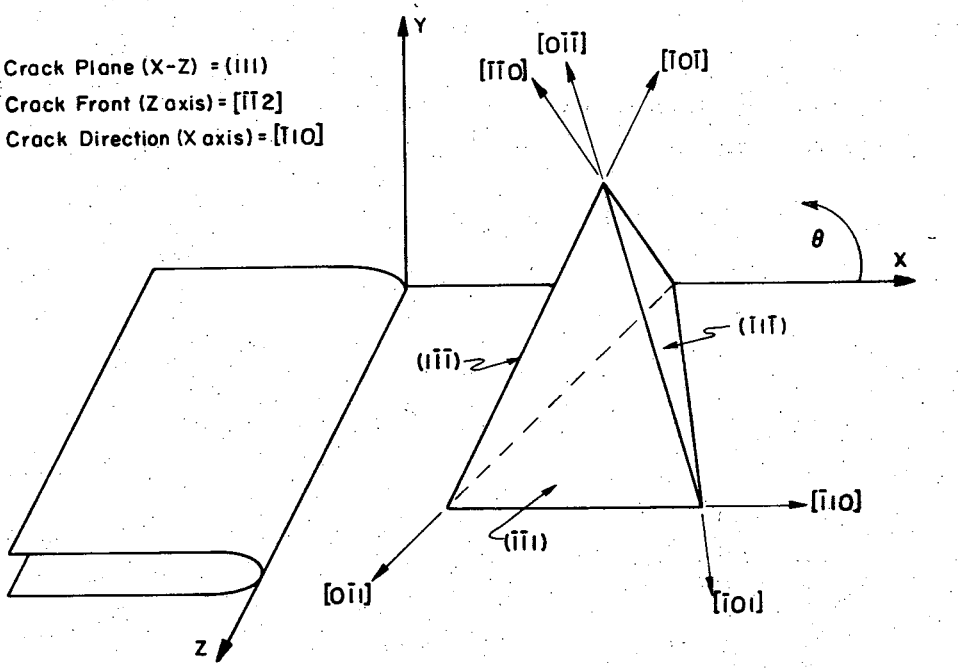
Crack Plane (X-Z) = (111)
Crack Front (Z axis) = [$\bar{1}\bar{1}$2]
Crack Direction (X axis) = [$\bar{1}$10]
Y
X
Z
θ
[$\bar{1}\bar{1}$0]
[0$\bar{1}\bar{1}$]
[$\bar{1}$0$\bar{1}$]
(1$\bar{1}\bar{1}$)
($\bar{1}$1$\bar{1}$)
($\bar{1}\bar{1}$1)
[$\bar{1}$10]
[0$\bar{1}$1]
[$\bar{1}$01]
XBL 718-7098

Fig. 2

Fig. 17. Surfanalyzer profile in the propagation direction of a room temperature fracture surface.

Fig. 18. Interference micrograph (Thallium green light) showing height of A type markings.

Fig. 19. Interference micrograph (Thallium green light) showing height of B type markings.

Fig. 20. Interference micrograph (Thallium green light) indicating height of corrugations.

Fig. 21. Instron load-deflection curves for a x-head speed of .0005 cm/min at three temperatures bracketing the brittle-ductile transition.

Fig. 22. Instron load-deflection curves for a x-head speed of .005 cm/min at three temperatures bracketing the brittle-ductile transition.

Fig. 23. Plot of stress intensity at fracture or flow versus temperature for five x-head speeds showing the respective brittle-ductile transition temperatures.

Fig. 24. X-ray topographs of the crack tip region in specimens whose load-deflection curves are shown in Fig. 21. (a) 699°C (b) 705°C (c) 707°C

Fig. 25. X-ray topographs of the crack tip region in specimens whose load-deflection curves are shown in Fig. 22. (a) 800°C (b) 801°C (c) 805°C

Fig. 26. Plot of log (x-head speed) versus $1/T_c$.

Fig. 27. Plot of $F(\theta)$ for each dislocation system on the $(\bar{1}\bar{1}1)$ glide plane under plane strain conditions.

Fig. 28. Plot of $F(\theta)$ for each dislocation system on the $(\bar{1}\bar{1}1)$ glide plane under plane stress conditions.

Fig. 29. Plot of $F(\theta)$ for each dislocation system on the $(\bar{1}1\bar{1})$ glide plane under plane strain conditions.

Fig. 30. Plot of $F(\theta)$ for each dislocation system on the $(\bar{1}1\bar{1})$ glide plane under plane stress conditions.

Fig. 31. Plot of $F(\theta)$ for each dislocation system on the $(1\bar{1}\bar{1})$ glide plane under plane strain conditions.

Fig. 32. Plot of $F(\theta)$ for each dislocation system on the $(1\bar{1}\bar{1})$ glide plane under plane stress conditions.

Fig. 33. Plot of $F(\theta)$ for each dislocation system on the (111) glide plane under plane strain conditions.

Fig. 34. Plot of $F(\theta)$ for each dislocation system on the (111) glide plane under plane stress conditions.

Fig. 35. X-ray topograph of a crack tip region along with a projection of the Thompson tetrahedron for $\bar{g} = [\bar{1}\bar{1}\bar{1}]$.

Fig. 36. X-ray topograph of a crack tip region along with a projection of the Thompson tetrahedron for $\bar{g} = [1\bar{1}\bar{1}]$.

Fig. 37. X-ray topograph of a crack tip region along with a projection of the Thompson tetrahedron for $\bar{g} = [\bar{1}1\bar{1}]$.

Fig. 38. X-ray topograph of a crack tip region along with a projection of the Thompson tetrahedron for $\bar{g} = [\bar{1}10]$.

Fig. 39. X-ray topograph of a crack tip region along with a projection of the Thompson tetrahedron for $\bar{g} = [110]$.

17. W. W. Mullins, "Metal Surfaces: Structure, Energetics and Kinetics", Joint Seminar of the ASM and the Met. Soc. of AIME, 26 (1962).

18. J. S. Vermaak and D. Kuhlmann-Wilsdorf, The Structure and Chemistry of Solid Surfaces, edited by G. A. Somorjai, John Wiley and Sons Inc, 75-1 (1968).

19. A. S. Tetelman and A. J. McEvily, Fracture of Structural Materials, (John Wiley and Sons, Inc., 1967) p. 49.

20. V. C. Kannan, "Direct Observation of Motion of Dislocations in Deformed Silicon by X-Ray Topography", Ph. D. Thesis, UCRL-18673, (1969).

21. P. C. Paris and G. C. Sih, "Fracture Toughness Testing and It's Applications", American Society for Testing and Materials, ASTM-STP 381, 32 (1965).

FIGURE CAPTIONS

Fig. 1. Specimen size and geometry along with the theoretical variation of the stress intensity after Srawley and Gross.

Fig. 2. Orientation between crack and specimen crystallography.

Fig. 3. Schematic of experimental setup for introducing cracks at root of machined notch.

Fig. 4. Schematic of fracture testing apparatus.

Fig. 5. Schematic of x-ray projection topograph arrangement.

Fig. 6. X-ray topograph of a precracked specimen.

Fig. 7. Photo micrograph of precrack fracture surface; Nomarski lens.

Fig. 8. Instron load-deflection curve without unloading for repetitive fracturing at room temperature.

Fig. 9. Instron load-deflection curve with unloading for repetitive fracturing at room temperature.

Fig. 10. (B/P) at crack extension versus (a/W) for one specimen at room temperature.

Fig. 11. (B/P) at crack extension versus (a/W) for all specimens at room temperature compared to the theoretical curve after Srawley and Gross for a γ of 2700 ergs/cm^2.

Fig. 12. (B/P) for both crack arrest and extension versus (a/W) for all specimens at room temperature.

Fig. 13. Variation of specimen compliance with (a/W) at room temperature.

Fig. 14. Photomicrograph of room temperature fracture surface; Nomarski lens.

Fig. 15. Photomicrograph of A type markings; Nomarski lens.

Fig. 16. Photomicrograph of B type markings; Nomarski lens.

Table VII

MILLER INDICES OF CRYSTALLOGRAPHIC DIRECTIONS
IN TERMS OF THE STRESS COORDINATE SYSTEM

Crystallographic Coordinates		Stress Coordinates	
Slip Plane	Slip Direction	Slip Plane	Slip Direction
$(1\bar{1}\bar{1})$	$[01\bar{1}]$	(-.817 -1.414 .577)	[-1.225 .707 0]
$(1\bar{1}\bar{1})$	$[\bar{1}0\bar{1}]$	(-.817 -1.414 .577)	[-.408 .707 1.154]
$(1\bar{1}\bar{1})$	$[\bar{1}\bar{1}0]$	(-.817 -1.414 .577)	[.817 0 1.154]
$(\bar{1}1\bar{1})$	$[0\bar{1}\bar{1}]$	(-.817 1.414 .577)	[-1.225 -.707 0]
$(\bar{1}1\bar{1})$	$[\bar{1}\bar{1}0]$	(-.817 1.414 .577)	[.817 0 1.154]
$(\bar{1}1\bar{1})$	$[10\bar{1}]$	(-.817 1.414 .577)	[-.408 -.707 1.154]
$(\bar{1}\bar{1}1)$	$[1\bar{1}0]$	(1.633 0 .577)	[0 -1.414 0]
$(\bar{1}\bar{1}1)$	$[0\bar{1}\bar{1}]$	(1.633 0 .577)	[-.408 .707 1.154]
$(\bar{1}\bar{1}1)$	$[\bar{1}0\bar{1}]$	(.633 0 .577)	[-.408 -.707 1.154]
(111)	$[1\bar{1}0]$	(0 0 1.732)	[0 -.414 0]
(111)	$[10\bar{1}]$	(0 0 1.732)	[-1.225 -.707 0]
(111)	$[01\bar{1}]$	(0 0 1.732)	[-1.225 .707 0]

REFERENCES

1. J. P. Hirth and J. Lothe, Theory of Dislocation, (McGrow-Hill Book, Inc., 1968).
2. H. Alexander and P. Haasen, Solid State Physics, 22 (1968).
3. I. V. Gridneva et al., Phys. Stat. Sol. 36, 59 (1969).
4. A. R. Lang, J. Appl. Phys., 30 No. 11, 1748 (1959).
5. A. S. Tetlman and W. D. Robertson, Acta Met, 11, 415 (1963).
6. M. Ge.. and W. D. Robertson, Acta Met, 14, 481 (1966).
7. S. J. Burns and W. W. Webb, J. Appl. Phys., 41 No. 5, 2078 (1970).
8. A. G. Evans, Phil. Mag., 22 No. 178, 841 (1970).
9. S. J. Burns, Acta Met, 18, 969 (1970).
10. W. D. Sylwestrowicz, Phil. Mag., 7 No. 8, 1825 (1962).
11. J. E. Srawley and B. Gross, "Stress Intensity Factors for Crackline-Loaded Edge-Crack Specimens", National Aeronautics and Space Administration, NASA TN D-3820.
12. A. R. Lang, "Recent Applications of X-Ray Topography", International Summer School University of Antwerp (1970).
13. E. S. Meieran, "The Application of X-Ray Topographical Techniques to the Study of Semiconductor Crystals and Devices", Fairchild Semiconductor Research and Development Laboratory Technical Report No. 400 (1969).
14. S. Mostovoy et al, J. of Mat'ls, 2, No. 3, 661 (1967).
15. J. J. Gilman, J. Appl. Phys., 31, 2208 (1960).
16. P. C. Parris and G. C. Sih, "Fracture Toughness Testing and It's Applications", American Society for Testing and Materials, ASTM STP 381, 72 (1965).

APPENDIX

Coordinate Transformation

The burger's vectors and the glide plane normal vectors may be transformed to the stress tensor coordinate system by the standard procedure if the direction cosines between the respective systems are known.

(ie) $X_i = a_{ij} \bar{X}_j$

$a_{ij} \equiv$ direction cosines

$\bar{X}_j \equiv$ crystallographic coordinates

$X_i \equiv$ stress tensor coordinates

The usual summation convention is assumed.

Table (6) lists the necessary data for the coordinate transformation and Table (7) shows the indices of the crystallographic directions in terms of the stress coordinate system.

Table VI

DIRECTION COSINES BETWEEN THE STRESS AND CRYSTALLOGRAPHIC COORDINATE SYSTEMS

$X_i \bar{X}_j$	Angle (acute)	Direction Cosine, A_{ij}
$X_1 \bar{X}_1$	65.90	.4083
$X_1 \bar{X}_2$	65.90	.4083
$X_1 \bar{X}_3$	35.15	-.8165
$X_2 \bar{X}_1$	45.00	-.7071
$X_2 \bar{X}_2$	45.00	.7071
$X_2 \bar{X}_3$	90.00	.0000
$X_3 \bar{X}_1$	54.74	.5772
$X_3 \bar{X}_2$	54.74	.5772
$X_3 \bar{X}_3$	54.74	.5772

IV. CONCLUSIONS

1. The surface energy of the {111} plane in dislocation-free silicon was determined to be about 2700-2800 ergs/cm^2 from both stress intensity and strain energy release rate analysis. The cause of the large discrepancy between this value and that found by Gilman's limited study was not established.

The theoretical variation of the stress intensity with crack length as calculated by Srawley and Gross via boundary collocation of the Williams form of stress function was verified experimentally.

2. The brittle to ductile transition for sharp cracks in silicon was found to occur within an extremely narrow temperature range, of the order of several degrees. The transition temperature was rate dependent over the temperature range studied (700-950°C) and obeyed a single activation energy of 1.9 eV. The activation energy thus obtained was shown to be related to the rate determining plasticity mechanism in the crack tip region and compared favorably with a value of 1.8 eV found in another study for kink-pair nucleation and glide.

No dislocations observable via x-ray topography were produced by mobile crack tips.

3. The force acting on each of the twelve glide systems emanating from the crack tip was calculated from isotropic elasticity theory and plotted as a function of angle about the crack front. The favored glide systems were derived from the force plots and compared to the operative glide systems as determined by x-ray topography. Good agreement between theory and experiment was obtained.

ACKNOWLEDGEMENTS

The author is very appreciative for the counsel and encouragement offered by Professor Earl Parker during the course of this investigation. My thanks are also due to Professor John Dorn for guidance on several occasions, Mrs. Shirley Ashley and Jean Wolslegel for typing the manuscript, Mrs. Gloria Pelatowski for preparation of the line drawings and Mrs. Phila Witherell for photographic printing.

This work was supported by the United States Atomic Energy Commission through the Inorganic Materials Research Division of the Lawrence Berkeley Laboratory.

Table V

FORCE RATIOS IN CONSTRAINED GLIDE DIRECTION FOR SYMMETRIC PLANES

Stress Condition	Slip System	Force Ratios	
		Front Lobes	Back Lobes
Plane Strain	$(\bar{1}1\bar{1})$;$[\bar{1}\bar{1}0]$:$[0\bar{1}\bar{1}]$:$[10\bar{1}]$	1.00/0.94/0.06	1.00/0.94/0.06
	$(1\bar{1}\bar{1})$;$[\bar{1}\bar{1}0]$:$[\bar{1}0\bar{1}]$:$[01\bar{1}]$		
Plane Stress	$(\bar{1}1\bar{1})$;$[\bar{1}\bar{1}0]$;$[0\bar{1}\bar{1}]$;$[10\bar{1}]$	1.00/0.59/0.41	0.52/1.00/0.48
	$(\bar{1}\bar{1}1)$;$[\bar{1}\bar{1}0]$:$[\bar{1}0\bar{1}]$:$[01\bar{1}]$		

and D have disappeared, the lobe at C has weakened, and the lobe at F is unchanged. The operative burger's vector(s) in the F lobe could be either or both the $[0\bar{1}\bar{1}]$ or/and the $[\bar{1}01]$ while in the C lobe the $[\bar{1}\bar{1}0]$ burger's vector is operative. Similarly in Fig. (37), the lobes have disappeared at C and F, weakened at D, and remained unchanged at E. The operative burger's vectors are thus $[\bar{1}0\bar{1}]$ or/and $[0\bar{1}1]$ at E and $[\bar{1}\bar{1}0]$ at D. In Fig. (38) lobes C and D weaken considerably which further indicates that the $[\bar{1}\bar{1}0]$ burger's vector is operative there. The individual dislocations in lobes C and D are difficult to resolve because of the overlapping $(\bar{1}\bar{1}1)$ glide plane systems at A and B. However, in Fig. (39) the $(\bar{1}\bar{1}1)$ systems are weakened and the dislocation segments in lobes C and D are resolved.

Except for the regions close to the crack tip where the multiplicity and overlapping of glide prevents analysis, the operative dislocation systems agree with those predicted by stress analysis.

(c) The (111) glide plane

Figures (33) and (34) show that in both plane strain and plane stress conditions the forces acting on all dislocation systems gliding in the fracture plane are zero. No dislocation activity is expected therefore on this glide plane and none was observed.

Table IV

EXTINCTION CONDITIONS (PURE SCREW)

$\bar{g}$	$\bar{b}$	$\lvert\bar{g}\cdot\bar{b}\rvert$	$\bar{g}$	$\bar{b}$	$\lvert\bar{g}\cdot\bar{b}\rvert$
$[\bar{1}\bar{1}\bar{1}]$	$[\bar{1}0\bar{1}]$	2	$[\bar{1}10]$	$[\bar{1}0\bar{1}]$	1
	$[0\bar{1}\bar{1}]$	2		$[0\bar{1}\bar{1}]$	1
	$[\bar{1}\bar{1}0]$	2		$[\bar{1}\bar{1}0]$	0
	$[0\bar{1}1]$	0		$[0\bar{1}1]$	1
	$[1\bar{1}0]$	0		$[1\bar{1}0]$	2
	$[\bar{1}01]$	0		$[\bar{1}01]$	1
$[1\bar{1}\bar{1}]$	$[\bar{1}0\bar{1}]$	0	$[110]$	$[\bar{1}0\bar{1}]$	1
	$[0\bar{1}\bar{1}]$	2		$[0\bar{1}\bar{1}]$	1
	$[\bar{1}\bar{1}0]$	0		$[\bar{1}\bar{1}0]$	2
	$[0\bar{1}1]$	0		$[0\bar{1}1]$	1
	$[1\bar{1}0]$	2		$[1\bar{1}0]$	0
	$[\bar{1}01]$	2		$[\bar{1}01]$	1
$[\bar{1}1\bar{1}]$	$[\bar{1}0\bar{1}]$	2			
	$[0\bar{1}\bar{1}]$	0			
	$[\bar{1}\bar{1}0]$	0			
	$[0\bar{1}1]$	2			
	$[1\bar{1}0]$	2			
	$[\bar{1}01]$	0			

Table (5). The front lobes are the sections of the cross-over pattern pointing in the positive X direction while the back lobes are those pointing in the negative X direction. Similar forces act on the two glide planes and are therefore grouped together. Plane strain conditions exist at the onset of plasticity and Table (5) indicates that in both the back and front lobes the $[\bar{1}\bar{1}0]$ burger's vector is favoured for both glide planes with the $[0\bar{1}\bar{1}]$ and $[\bar{1}0\bar{1}]$ burger's vectors slightly less favoured in the $(\bar{1}1\bar{1})$ and $(1\bar{1}\bar{1})$ glide planes respectively. However, in the initial stages of flow when the lobes are close to the crack tip, the angular variation about which dislocations may glide is not closely restricted to the intersection of the glide planes and the specimen surface. After considerable flow has occurred the stress conditions will be better approximated by plane stress and the lobes will have extended such that the angular variation for glide is small. Table (5) indicates that under plane stress conditions the $[\bar{1}\bar{1}0]$ burger's vector is favoured in the front lobes and the $[0\bar{1}\bar{1}]$ and $[\bar{1}0\bar{1}]$ burger's vectors are favoured in the back lobes for the $(\bar{1}1\bar{1})$ and $(1\bar{1}\bar{1})$ glide planes respectively. Therefore, from stress considerations only, one would expect to find multiple slip systems operating in all lobes close to the crack tip due to the initial plane strain condition and large angular variations available. Further from the crack tip the front lobes should have predominantly $[\bar{1}\bar{1}0]$ burger's vectors and the back lobes $[0\bar{1}\bar{1}]$ and $[\bar{1}0\bar{1}]$ burger's vectors for the $(\bar{1}1\bar{1})$ and $(1\bar{1}\bar{1})$ glide planes respectively.

Figure (35) shows the back and front facing lobes where glide systems on the $(\bar{1}1\bar{1})$ plane operate between C-F and those on the $(1\bar{1}\bar{1})$ operate between D-E. The angle between C-F and D-E is as predicted indicating that no cross-slip has occured. In Fig. (36) the lobes at E

extensive plastic flow, because of overlapping glide systems. However, the dislocation identification experiments were somewhat simplified because of the tendency for dislocation segments to lie along the Peierls valleys (the < 110 > directions) at the temperatures encountered in this study. All topographs are therefore accompanied with a suitable projection of the Thompson tetrahedron thereby allowing the direction of the dislocation segments to be determined by inspection. Only one specimen is examined here but many observations indicate that the same slip systems are operative at all the test temperatures.

(a) The $(\bar{1}\bar{1}1)$ glide plane

Figures (27) and (28) show similar stress functions for burger's vectors $[\bar{1}0\bar{1}]$ and $[0\bar{1}\bar{1}]$ under plane strain and plane stress conditions respectively. The third, multi-lobed, stress function for the burger's vector $[\bar{1}10]$ is considerably less important than the first two functions. This difference in magnitude increases while going from plane strain to plane stress conditions as the plastic zone increases. The two favoured glide systems have their maximum force in advance of the crack tip and on opposite sides of the fracture plane. The multi-lobed glide system is doubly unfavoured because of the force reversals in adjacent lobes which constrain dislocations of a particular sign to expand within a narrow angular range.

Figure (35) is an x-ray topograph of the crack tip region with an operating $\bar{g}$ vector equal to $[\bar{1}\bar{1}\bar{1}]$. Two dislocation systems, both with segments in the [011] and [101] directions, are visible ahead of the crack at A and B. The simultaneous presence of these two directions in any one dislocation system means that the glide plane is $(\bar{1}\bar{1}1)$. Further, only the $(\bar{1}\bar{1}1)$ plane which lies at a low angle to the specimen surface

could allow slip of such width to occur. Table (4) shows that of the burger's vectors present in the $(\bar{1}\bar{1}1)$ glide plane, both $[\bar{1}0\bar{1}]$ and $[0\bar{1}\bar{1}]$ are equally visible while $[1\bar{1}0]$ is invisible for pure screw. Figures (36) and (37) are topographs with operating $\bar{g}$ vectors of $[1\bar{1}\bar{1}]$ and $[\bar{1}1\bar{1}]$ respectively. The glide system at A in Fig. (35) has disappeared in Fig. (37) while the one at B has remained. Conversely, the system at B has disappeared in Fig. (36) while A remained. Table (4) shows that for Fig. (37) only dislocations in the $(\bar{1}\bar{1}1)$ glide plane with a burger's vector of $[\bar{1}0\bar{1}]$ should be visible while for Fig. (36) only those dislocations in the $(\bar{1}\bar{1}1)$ plane with a burger's vector of $[0\bar{1}\bar{1}]$ should be visible. It can therefore be concluded that the system at A has a burger's vector of $[0\bar{1}\bar{1}]$ and the system at B has a burger's vector of $[\bar{1}0\bar{1}]$. The dislocation segments closest to the fracture plane are in screw orientation the others are in the 60° orientation. The 60° segments do not obey the $\bar{g} \cdot \bar{b}$ bisibility criterion completely because of their edge component as seen in Fig. (37).

The physical situation existing on the $(\bar{1}\bar{1}1)$ glide plane agrees completely with that predicted by theory.

(b) The $(\bar{1}1\bar{1})$ and $(1\bar{1}\bar{1})$ glide planes

The force functions for the dislocation systems gliding on the $(\bar{1}1\bar{1})$ and $(1\bar{1}\bar{1})$ planes are shown in Figs. (29) to (32). These two planes are examined together since they lie symmetrically with respect to the crack front and therefore have similar force fields. Both planes make a steep angle with the specimen surface and any glide originating from the crack tip is restricted to narrow bands that make a characteristic cross-over, as shown in Fig. (35). The relative magnitudes of the forces acting on each slip system in the direction of the constrained glide are shown in

Table II

ANGULAR STRESS FUNCTION
FOR PLANE STRESS

Slip System	$F_i(\theta)$
$(1\bar{1}\bar{1})$ $[01\bar{1}]$	$[.408A - 3C(1 - B)]$
$(1\bar{1}\bar{1})$ $[\bar{1}0\bar{1}]$	$[-1.225A - C(1 - 5B)]$
$(1\bar{1}\bar{1})$ $[\bar{1}\bar{1}0]$	$[-1.633A + 2C(1 + B)]$
$(\bar{1}1\bar{1})$ $[0\bar{1}\bar{1}]$	$[1.225A - C(1 - 5B)]$
$(\bar{1}1\bar{1})$ $[\bar{1}\bar{1}0]$	$[1.633A + 2C(1 + B)]$
$(\bar{1}1\bar{1})$ $[10\bar{1}]$	$[-.408A - 3C(1 - B)]$
$(\bar{1}\bar{1}1)$ $[1\bar{1}0]$	$[-.816A]$
$(\bar{1}\bar{1}1)$ $[0\bar{1}\bar{1}]$	$[-.408A + 2C(1 + B)]$
$(\bar{1}\bar{1}1)$ $[\bar{1}0\bar{1}]$	$[.408A + 2C(1 + B)]$
(111) $[1\bar{1}0]$	$[-2.450A]$
(111) $[10\bar{1}]$	$[-1.225A]$
(111) $[01\bar{1}]$	$[1.225A]$

where $A = \sin\theta/2 \ \cos\theta/2 \ \cos 3\theta/2$

$B = \sin\theta/2 \ \sin 3\theta/2$

$C = \dfrac{\cos\theta/2}{3}$

Table III

ANGULAR STRESS FUNCTION
FOR PLANE STRAIN

Slip System	$F_i(\theta)$
$(1\bar{1}\bar{1})$ $[01\bar{1}]$	$[.408 - 3C(.556 - B)]$
$(1\bar{1}\bar{1})$ $[\bar{1}0\bar{1}]$	$[-1.225A - C(.556 - 5B)]$
$(1\bar{1}\bar{1})$ $[\bar{1}\bar{1}0]$	$[-1.633A + 2C(.556 + B)]$
$(\bar{1}1\bar{1})$ $[0\bar{1}\bar{1}]$	$[1.225A - C(.556 - 5B)]$
$(\bar{1}1\bar{1})$ $[\bar{1}\bar{1}0]$	$[1.633A + 2C(.556 + B)]$
$(\bar{1}1\bar{1})$ $[10\bar{1}]$	$[-.408A - 3C(.556 - B)]$
$(\bar{1}\bar{1}1)$ $[1\bar{1}0]$	$[-.816A]$
$(\bar{1}\bar{1}1)$ $[0\bar{1}\bar{1}]$	$[-.408A + 2C(.556 + B)]$
$(\bar{1}\bar{1}1)$ $[\bar{1}0\bar{1}]$	$[.408A + 2C(.556 + B)]$
(111) $[1\bar{1}0]$	$[-2.450A]$
(111) $[10\bar{1}]$	$[-1.225A]$
(111) $[01\bar{1}]$	$[1.225A]$

where $A = \sin\theta/2 \ \cos\theta/2 \ \cos 3\theta/2$

$B = \sin\theta/2 \ \sin 3\theta/2$

$C = \dfrac{\cos\theta/2}{3}$

2. Dislocation Configurations at the Crack Tip

The extent and shape of the plastic zone produced from the crack tip is predicated by the crystallographic relationship between the crack and the operative slip systems. The spatial distribution of the force exerted on each of the twelve slip systems may be obtained from the isotropic elasticity theory of stress concentrations. The use of isotropic elasticity is reasonable since silicon has a low anisotropic factor. Any refinement obtained through using anisotropic elasticity theory would not be worth the considerable difficulty involved.

The force per unit length acting normal to a dislocation with burger's vector, $\bar{b}$, and gliding on a plane with normal, $\bar{n}$, under the influence of a stress tensor $\bar{\sigma}$ is given by;

$$F = b_i \cdot \sigma_{ij} \cdot n_j \qquad i,j = 1, 2, 3$$

The usual summation convention is implied.

The stress tensor applicable to this study is given by,[21]

$$\sigma_{xx} = \frac{K_I}{\sqrt{2\pi r}} \text{Cos } \theta/2 \, [1 - \text{Sin } \theta/2 \text{ Sin } 3\theta/2]$$

$$\sigma_{yy} = \frac{K_I}{\sqrt{2\pi r}} \text{Cos } \theta/2 \, [1 + \text{Sin } \theta/2 \text{ Sin } 3\theta/2]$$

$$\sigma_{zz} = 0 \quad \text{(plane stress)}$$

or $$\sigma_{zz} = (\sigma_{xx} + \sigma_{yy}) \quad \text{(plane strain)}$$

$$\sigma_{xy} = \sigma_{yx} = \frac{K_I}{\sqrt{2\pi r}} \text{Sin } \theta/2 \text{ Cos } \theta/2 \text{ Cos } 3\theta/2$$

$$\sigma_{xz} = \sigma_{zx} = \sigma_{yz} = \sigma_{zy} = 0$$

The orientation of the (xyz) coordinate system relative to the crack front and the specimen crystallography is shown in Fig. (1). Since the stress tensor coordinate system and the crystallographic coordinate

system do not coincide the crystallographic system must be redefined in terms of the stress tensor system. This is done in the Appendix.

The calculation of the force per unit length for each slip system may now be carried out directly according to the preceding relationships. The resultant force fields all have the same general form,

$$F_i = \frac{a}{\sqrt{6}} \frac{K_I}{\sqrt{2\pi r}} F_i(\theta) \qquad i = 1, 2, \ldots. 12$$

a ≡ lattice parameter

r and θ are polar coordinates

Tables (2) and (3) list the angular functions, $F_i(\theta)$, for all twelve slip systems under plane stress and plane strain conditions respectively. For any fixed radial distance, r, from the crack tip, the relative intensities of the forces exerted on each dislocation type may be compared as a function of angle. The angular functions are shown in polar form in Figs. (27) through (34) with the absolute value of the function plotted radially from the origin. The positive lobes represent a repulsion of the dislocation, as defined by the sense of the burger's vector, from the crack tip; negative lobes being attractive to the crack tip. The force plots are grouped according to slip plane and stress condition. The projection of the slip planes that make a steep angle with the specimen surface on the X-Y plane is superimposed so as to indicate how the dislocations gliding out from the crack tips are constrained.

The following sections are a detailed comparison of the operative slip systems as determined experimentally via x-ray topography to those slip systems that are theoretically favoured. There was some difficulty in resolving the dislocations closest to the crack tip, especially after

n = constant

C = constant that is weakly temperature dependent compared to the exponential term

G = activation energy of the rate determining process

At the critical temperature, T_c;

$$\frac{d\,\sigma_{yy}^{max}}{dt} = \frac{-AC\left[B\rho^{1/2} + 1/2(\delta - B\rho)\rho^{-1/2}\right]}{C_E\,\rho}\,\sigma_c^n\,e^{-G/kTc}$$

$$+ \frac{A}{C_E\,\rho^{1/2}}\left(\frac{d\delta}{dt}\right)$$

$$= 0$$

or,

$$\left(\frac{d\delta}{dt}\right) = \frac{BC}{2}\left[1 + \delta/\delta_p\right]\sigma_c^n\;e^{-G/kTc}$$

If all the pre-exponential terms in the above relation vary relatively weakly with temperature, then the usual Arrhenius activation energy plot may be invoked. Figure (26) shows that the critical temperature and the applied x-head speed are related exponentially by a single activation energy over the temperature range concerned. The activation energy derived from Fig. (26) is 1.9 eV which compares well with value of 1.8 eV found by Kannan[20] for glide of screw and 60° dislocations in silicon at similar temperatures. Theoretically, the activation energy for glide in a solid with a large Peierls barrier represents the arithmetic mean of the activation energies for kink-pair nucleation and migration.

An estimation of whether the "punching-out" of dislocations at the crack tip is rate dependent or not at stresses in the vicinity of σ_c may be obtained by comparing the dislocation line energy necessary to create a circular loop with the work done on the loop by the crack tip stress

field. In the initial stages of plasticity the shear stress field may be approximated by the elastic solution,

$$\tau \simeq \frac{K_I}{\sqrt{2\pi r}}\;f(\theta)$$

where r is the radial distance from the crack tip and the angular function, $f(\theta)$, may be set at unity.

The work done by the shear stress field on expanding a circular loop is therefore;

$$W = \sqrt{2\pi}\;b\,K_I\int_0^R R^{1/2}\,dR$$

$$= 2/3\,\sqrt{2\pi}\,K_I\,b\,R^{3/2}$$

where, b ≡ burger's vector, 3.84×10^{-8}cm

R ≡ loop radius

Note that the work term varies with the 3/2 power for a crack tip stress field as opposed to 2 power for a constant shear stress.

The energy associated with the dislocation line energy is given by[1],

$$E = 1/2\,\frac{(2-\nu)}{(1-\nu)}\,\mu\,b^2\,R\,[\ln 4R/R_o - 2]$$

where μ ≡ shear modulus; 6.4×10^{11} dynes/cm^2

R_o ≡ dislocation core radius, about equal to b.

The activation energy for dislocation nucleation at the crack tip is the maximum with respect to the loop radius of the term [E(R) - W(R)]. If W(R) is always greater than E(R) then the process is spontaneous and not rate dependent. For a K_{Ic} of about 10^8 dynes/cm^2 it can easily be shown that for stress intensities greater than about 10 per cent of K_{Ic} the dislocation nucleation process at the crack tip is not rate dependent. One would tend to conclude therefore that the rate controlling step is dislocation glide rather than nucleation.

$$\sigma_{yy} = \frac{2K_I}{\sqrt{\pi}} \left(\frac{1}{\rho + 4r} \right)^{1/2}$$

where $K_I \equiv$ stress intensity and is essentially independent of crack length for this analysis

thus $K_I = AP$ A is a constant

$\rho \equiv$ crack tip radius

$r \equiv$ radial distance from crack tip

The maximum stress acting on the fracture plane is therefore a function only of the applied load and the crack tip radius,

$$\sigma_{yy}^{max} = \frac{AP}{\rho^{1/2}}$$

where ρ has a minimum value of the same order of magnitude as the lattice spacing.

A necessary and sufficient condition for fracture to occur is that the maximum normal stress exceed some critical value,

$$\sigma_{yy}^{max} \geqslant \sigma_c$$

where σ_c is a constant property of the material and in this case is related to the surface energy. Therefore, as the specimen loading points are displaced at a constant rate, the variation of the ratio of P to $\rho^{1/2}$ will be determined by the amount of plasticity occurring at the crack tip. The plasticity is a function of temperature for a rate sensitive solid such as silicon. At any temperature below a critical temperature, T_c, the maximum normal stress, σ_{yy}^{max}, will increase with time for a particular x-head speed until the critical stress is exceeded and fracture ensues. The amount of plasticity that takes place before fracture will depend on the temperature difference, $(T_c - T)$. Above T_c, σ_{yy}^{max} will experience a maximum value with time that is always less than

σ_c and the specimen will deform plastically without fracturing. The conditions, therefore, that determine the critical temperature for a particular crosshead speed are,

(i) $\sigma_{yy}^{max} = \sigma_c$

(ii) $\frac{d\,\sigma_{yy}^{max}}{dt} = 0$ when $\sigma_{yy}^{max} = \sigma_c$

Under fixed grip conditions, the displacement at the point of loading, δ, may be expressed in terms of elastic and plastic components,

$$\delta = \delta_E + \delta_p$$

where $\delta_E = C_E P$

$C_E \equiv$ elastic compliance, essentially constant with temperature

and $\delta_p = B\rho$

$B \equiv$ a constant relating the displacement at the point of loading due to plastic enlargement of the crack tip radius, ρ, to the crack tip radius

Therefore;

$$\sigma_{yy}^{max} = \frac{A\,(\delta - B\rho)}{C_E\,\rho^{1/2}}$$

and

$$\frac{d\,\sigma_{yy}^{max}}{dt} = \left.\frac{\partial\,\sigma_{yy}^{max}}{\partial\rho}\right|_{\delta} \frac{d\rho}{dt} + \left.\frac{\partial\,\sigma_{yy}^{max}}{\partial\delta}\right|_{\rho} \frac{d\delta}{dt}$$

where

(i) for any x-head speed and a "hard" machine, $\left(\frac{d\delta}{dt}\right)$ is a constant

(ii) $\frac{d\rho}{dt} = C \left[\sigma_{yy}^{max}\right]^n e^{-G/kT}$

(ie) the crack tip enlargement rate is related to a thermally activated mechanism with,

C. High Temperature Results

1. Brittle to Ductile Transition

The most important and remarkable feature of the high temperature fracture results was the extremely narrow brittle to ductile temperature range and the dependence of the transition temperature range on strain rate. Absolutely no slow crack growth was observed which precluded any attempt to correlate directly the strain energy release rate with plastic work. However, the absence of slow crack propagation combined with the extremely narrow transition temperature range gave considerable information on the energetics of dislocation formation and/or motion in the crack tip region.

Figures (21) and (22) show the load-deflection curves for two strain rates and for temperatures that encompass their respective brittle to ductile transitions. It can be seen that the fracture load increases rapidly from values typical of room temperature fracture within a temperature range of several degrees. At a certain critical temperature, fracture does not occur and the applied load appears to increase indefinitely with accompanying plastic flow as for example the 707°C specimen in Fig. (21). Slightly above this critical temperature, the applied load goes through a maximum value as for example the 805°C specimen in Fig. (22). The results of 29 specimens tested at five strain rates are shown in Fig. (23) where the open symbols represent the stress intensity at fracture and the closed symbols represent the maximum stress intensity attained during plastic flow. The use of the stress intensity in this plot accommodates any variation in specimen thickness or crack length. The stress intensity calculations are based on the premise that the crack tip is sharp which is not the case after considerable plastic flow has occurred. However, Fig. (23) serves to illustrate the extreme

abruptness of the transition from complete brittleness to complete plasticity and the variation of the transition temperature with strain rate.

X-ray topographs were taken of most of the high temperature test specimens in order to evaluate the extent and form of the plastic flow in the crack tip region. Figures (24) and (25) are x-ray topographs of the same specimens whose load-deflection curves are shown in Figs. (21) and (22). The rapid increase in load at fracture is shown to be accompanied by a sharp increase in plastic zone size from essentially zero in Fig. (24-a) and Fig. (25-a) to substantial in Fig. (24-b) and Fig. (25-b). It can be seen from the four above-mentioned topographs that no plastic flow has occurred during crack propagation. Figure (24-c) and Fig. (25-c) show the extensive dislocation activity on the glide planes emanating from the crack tip and that essentially all plasticity is associated with the crack tip region.

The strain rate sensitivity of the well-defined brittle to ductile transition temperature may be utilized to estimate the energetics of the rate controlling plasticity mechanism operating in the crack tip region. This mechanism could be either the "punching-out" of dislocations from the crack tip since the undeformed silicon is dislocation free or the subsequent glide of the dislocations thus produced down their respective force fields radiating out from the crack tip.

When considering the conditions that lead to either fracture or plasticity one needs only to determine the effect of plasticity on the stress normal to the fracture plane adjacent to the crack tip. It can be shown that a good approximation for the stress acting on the fracture plane close to the crack tip is,[19]

somewhere between the two extreme values for crack extension and crack arrest. An exact calculation of the surface energy may be obtained if the strain energy release rate is integrated over the length of any particular crack jump thereby eliminating the need to account for any transient kinetic energy term. A simple relationship is developed here for the calculation of the total or integrated strain energy released during a crack jump;

$$G = \frac{P^2}{2B} \frac{\partial c}{\partial a}$$

$$\equiv \frac{\partial U}{\partial a}$$

where

$$U \equiv \text{elastic strain energy}$$

Under fixed grip conditions and when the applied deflection rate is small compared to the crack extension rate, the specimen deflection at the point of loading is constant during the crack jump. Therefore;

$$Pc = \delta$$

where δ is constant and,

$$\frac{\partial U}{\partial a} = \frac{\delta^2}{2B} \frac{1}{c^2} \frac{\partial c}{\partial a}$$

Therefore;

$$\Delta U_i^{i+1} = \frac{\delta^2}{2B} \int_{c_i}^{c_{i+1}} \frac{dc}{c^2}$$

where δ is given by either $(P_i\, c_i)$ or $(P_{i+1}\, c_{i+1})$. The surface energy is given by,

$$\gamma = \frac{\Delta U_i^{i+1}}{2\Delta a_i^{i+1}}$$

Calculations based on the above relationship and in regions where the compliance is sufficiently linear give surface energy values that lie midway between those for crack start and crack arrest.

A point that is generally ignored in surface energy studies of solids is the variation of surface energy with strain in the bulk. This dependency accounts for the difference between surface stress, f, and surface energy, γ, and whose interrelationship can easily be shown to be,[17]

$$f_{ij} = \delta_{ij}\, \gamma + \frac{\partial \gamma}{\partial \varepsilon_{ij}} \qquad i,j = 1,2$$

where

$$\delta_{ij} = 1 \qquad \text{if } i = j$$
$$= 0 \qquad \text{if } i \neq j$$

i refers to a plane perpendicular to the surface

j refers to the direction in the surface and perpendicular to the i plane.

The term $\frac{\partial \gamma}{\partial \varepsilon_{ij}}$ can be of the same order of magnitude as γ and in one study[18] was found to be negative. The fact that the surface energy decreased with increasing strain was thought to be the result of the compressive state of the surface atoms. This variation of surface energy with strain could possibly lead to a non-negligible variation of surface energy with crack length.

Gilman's study was carried out at -196°C and a variation in the surface energy between this temperature and 20°C is conceivable. A substantial change appears improbable however since the surface energy determined by this work remained almost constant between 20°C and 950°C.

typical overall appearance of the fracture surfaces. Three different types of surface markings are visible at A, B, and C. The markings at A are well-defined lines extending across the specimen width and are perpendicular to the crack propagation direction. An example of this marking is shown in greater detail in Fig. (15). A comparison of these lines and the number of fracture starts indicated by the Instron recorder showed a one to one correspondence. It was therefore assumed that these lines marked the static positions of the crack front. The much fainter lines indicated at B in Fig. (14) are shown in more detail in Fig. (16). The third type of markings were faint lines spaced about one micron apart running parallel with the crack propagation direction. These markings formed a corrugated surface whose amplitude appeared to decrease from crack initiation to crack arrest as shown in Fig. (15).

An examination of the fracture surface profile was conducted since the surface energy calculation could be substantially affected if the crack path deviates greatly from the plane of maximum tensile stress, in this case the (111), or if the effective surface area is increased by the surface corrugations. A surface profile is shown in Fig. (17) with the vertical scale greatly exaggerated. The profile was made parallel to the crack propagation direction and thereby illustrates the difference between the A and B type markings. The fainter B lines represent steps between relatively long lengths of crack surface of different elevation. These steps change the surface elevation by about 100 to 200 A° over a horizontal distance of 10 to 15 microns. The well-defined or A type markings are basically the same as the faint markings only the elevation change of the former is about 800 to 1000 A°. The step heights as measured by the surfanalyser were corroborated by interference microscopy as

shown in Fig. (18) for the well-defined markings and in Fig. (19) for the faint markings. The angular deviation from the fracture plane for both types of steps is of the order of one degree and therefore it must be concluded that these temporary deviations during the first 10 microns of crack extension are not significant enough to alter the surface energy calculation. Slight loading eccentricities could be the cause of these markings.

The surface corrugations were too closely spaced to allow a surface profile to be taken, however, interference microscopy indicates that the depth of the corrugation is about 200A° as shown in Fig. (20). The increase in fracture surface area due to this type of surface marking is therefore negligible.

One can conclude from the examination and analysis of all the surface markings that the apparently high value of the fracture surface energy found by this work is not due to the surface morphology.

4. Other Surface Energy Considerations

The usual criterion that the strain energy released must equal the surface energy produced (for fixed grips) is certainly a necessary condition but not necessarily a sufficient condition for crack extension in the absence of plasticity. There may exist for example a critical stress at the crack tip that must be satisfied to enable crack extension. In this case the strain energy release rate may exceed the surface energy absorption rate and the excess energy thereby generated would appear in the form of kinetic energy. This is apparently the case in this study since the crack extension energy release rates are greater by a factor of about 15 percent than the respective rates for crack arrest. The true values that should be used in any surface energy calculation lie

Table I

SURFACE ENERGIES OBTAINED FROM COMPLIANCE DATA FOR CRACK EXTENSION AND ARREST

Fracture	$a_i - a_{i+1}$ (mm)		$\partial c/\partial a (10^{-3}/kg)$		P(kg)		γ(ergs/cm^2)	
	Start	Arrest	Start	Arrest	Start	Arrest	Start	Arrest
1	12.23	14.38	(1.20)	(1.45)	.825	.660	(2100)	(1600)
2	14.38	16.88	1.45	1.88*	.832	.720	2540	2480*
3	16.88	19.13	1.88*	2.23*	.782	.672	2910*	2560*
4	19.13	20.23	2.23*	3.00	728	.651	3000*	3230
5	20.23	Total length	3.00	———	.690	———	3600	———

extrapolation and are therefore considered the most reliable. The values marked with brackets are a complete extrapolation while the unmarked values involve a partial extrapolation.

The average of sixteen surface energy values obtained by the strain energy release rate approach was 2870 ergs/cm^2. This value agrees well with the value of 2700 ergs/cm^2 resulting from the stress intensity approach.

The fact that the stress intensity and strain energy release rate calculations agree provides a basis for confidence in the surface energy value obtained from this study. However, the value that is generally quoted in the literature is 1350 ergs/cm^2 (when corrected for the Young's modulus assumed in this study) and originates from a study by Gilman[15] who utilized a crystal cleavage technique similar to that of this study. The two specimens cleaved in Gilman's experiments had a trouser-leg configuration of constant cross-section and produced just one fracture each. The strain energy release rate was obtained via the standard cantilever beam approximation for this type of specimen configuration. As a control, the appropriate data listed by Gilman were applied by this student to the pertinent stress intensity relation[16] and the resulting surface energy values agreed very closely with those listed by Gilman. Gilman's value for silicon thus appears to be reasonable and it remains to be shown why the surface energy values obtained from this work are about twice as large.

3. Fracture Surface Morphology

The fracture surfaces were examined with the light microscope and Nomarski interference-contrast lens since the scanning electron microscope failed to resolve surface detail. Figure (14) illustrates the

in Fig. (1). The K_{Ic} was not found to vary with crack length which implies that the stress intensity as a function of crack length is close to that predicted by theory for this particular specimen shape. The average K_{Ic} value was found to be 9.37×10^7 dynes/cm$^{3/2}$. The K_{Ic} may be related to the strain energy release rate which in turn is equated to the fracture surface energy produced in the case of a completely elastic fracture.

$$G_{Ic} = \frac{K_{Ic}^2 (1-\upsilon^2)}{E}$$
$$= 2\gamma$$

or

$$\gamma = \frac{K_{Ic}^2 (1-\upsilon^2)}{2E}$$

where G_{Ic} ≡ critical strain energy release rate

γ ≡ fracture surface energy

υ ≡ Poisson's ratio, 0.215

E ≡ Young's modulus, 15.5×10^{11} dynes/cm^2

The surface free energy associated with the crack extension data is thus calculated to be 2700 ergs/cm^2 with a standard deviation of 150 ergs/cm^2.

A similar analysis may also be applied to the crack arrest data. However the load measurements at crack arrest were somewhat less accurate than those for crack extension due to the overshooting of the chart recorder pen. The crack arrest loads were obtained by extrapolating the reload curves back through the vertical sections of the load curve. The crack arrest data for all specimens are plotted in Fig. (12) along with a least squares polynomial curve fit (polynomial of degree three). The least squares polynomial curve fit for the crack extension data is also shown in Fig. (12) to illustrate the lower K_{Ic} values associated with crack arrest. A calculation similar to that made for the critical strain

energy release rate for crack extension was applied to the crack arrest data which yielded a surface free energy of 2300 ergs/cm^2.

The ratio of the surface free energies for crack arrest and crack extension is therefore;

$$\gamma \text{ crack arrest}/\gamma \text{ crack start} = 0.85$$

2. Strain Energy Release Rate Approach

An alternative and equivalent method of evaluating the fracture surface energy is to determine the strain energy release rate directly from the experimental data using the well known relationship;[14]

$$G_{Ic} = \frac{P^2}{2B} \frac{\partial c}{\partial a}$$

where

a ≡ crack length

c ≡ specimen compliance

P ≡ load at fracture

B ≡ specimen width

A typical variation of compliance with crack length is shown in Fig. (13). The compliance decreases from the first to the second crack position which is clearly spurious since the compliance should always increase with crack length. The data points associated with the initial or precrack position were therefore ignored for curve fitting purposes. Table (1) shows the pertinent data obtained from Fig. (13) and from the Instron recorder along with the resultant surface energies as calculated from the preceding relationship. The surface energies thus calculated increase gradually with crack length which is consistent with the results obtained from all the other specimens so analysed. The values in Table (1) marked with an asterisk are those that did not involve any

III RESULTS AND DISCUSSION

A. Precracking

The precracking technique proved to be remarkably effective both in stopping cracks at the desired location and in producing reasonably uniform crack surfaces. The technique was one hundred percent reliable for the series of fifty specimens used in this study.

The point during loading at which a crack initiated from the machined notch was easily seen from the sudden load drop on the Instron chart recorder. The x-head travel direction could be reversed before any subsequent loading occured due to the slow speeds involved which in turn were effectively further reduced by a factor of five because the wedge taper.

The precrack lengths ranged from 3 mm to 8 mm with an average of about 6 mm. Figure (6) shows an x-ray topograph of a typical precracked specimen where the (111) fracture plane is seen at a glancing angle of about 6.5 degrees. The deviation of the fracture surface from the desired (111) fracture plane could be estimated from the projected width of the crack and usually amounted to several degrees. The deviation along the length of the precrack was of a similar magnitude. These slight deviations from the theoretical fracture plane were presumed to be due to loading eccentricities. Figure (7) is an optical micrograph of the fracture surface and shows a typical precrack morphology. The precrack surfaces were always much more irregular than the fracture surfaces subsequently produced by the Mode I pin loaded configuration. Occasionally the precrack showed twisting and ridge formations which acted as secondary stress raisers for dislocation nucleation at high temperatures.

B. Room Temperature Tests

The room temperature tests were performed mainly to establish the strain energy release rate and stress intensity necessary to initiate crack extension under completely elastic conditions. A secondary objective was to corroborate experimentally the theoretical variation of the stress intensity with crack length as predicted by Srawley for the particular specimen configuration used in this study.

These tests were carried out at the slowest Instron cross-head speed available; 5 microns per minute. At this deflection rate the specimens exhibited repetitive cracking which ranged from several to eight fractures per specimen. Figure (8) shows the Instron load-deflection curve for a specimen with six fracture starts. Several specimens were unloaded after each crack extension so as to facilitate compliance measurements, as shown in Fig. (9).

1. Stress Intensity Approach

Figure (10) shows a plot of the fracture initiation data, (B/P) versus (a/W), for one specimen. It can be seen that the curve has the same form as that predicted by theory and shown in Fig. (1) except for the initial fracture extending from the precrack. This anomaly occurred in about one half of the specimens. All the data points for the eight specimens are shown in Fig. (11) along with a least squares polynomial fit (polynomial of degree three). No trend was found in the data for specimens varying either plus or minus fifty percent from the normal thickness of 1 mm. This indicates that plane strain conditions may be assumed to prevail at room temperature.

K_{Ic} as a function of crack length may be derived from a comparison of the experimental curve of Fig. (11) to Srawley's theoretical curve

arrested. The crack arest position could be varied by adjusting the applied compressive load.

2. Fracture Testing

The tensile fracture testing arrangement is shown in Fig. (4). Since the testing was done in air, all structural components exposed to high temperatures were fabricated from Inconel 600, except for the specimen loading pins which were of alumina. The loading arrangement was designed to be lowered into a heating device which was for this study a cylindrical electric resistance furnace that could be closed off to air circulation. As shown in Fig. (4), the specimens were closely shielded by two loading members so as to promote a uniform temperature zone along the fracture path. The temperature control was within ±0.5°C.

C. X-ray Topography

There exist many arrangements for the observation of defects in crystalline solids with x-ray topography. Several comprehensive review articles on both theory and experimental procedure have been recently made available.[12,13] This study makes use of the most commonly used technique known as projection topography. The camera arrangement is shown in Fig. (5). After being positioned to a Bragg reflection, $\bar{g}$, the specimen and film may be oscillated synchronously across the impinging x-ray beam so that relatively large specimen areas may be examined.

Since this study utilized primary extinction conditions, screw dislocations are therefore invisible when $\bar{g} \cdot \bar{b} = 0$ while edge dislocations are invisible when both $\bar{g} \cdot \bar{b} = 0$ and $\bar{g} \times \bar{n} = 0$, where $\bar{g}$ is the operating diffraction vector, $\bar{b}$ is the dislocation burger's vector, and $\bar{n}$ is the tangent to the dislocation line.

All topographs were taken with a Hilger micro-focus unit operating in conjunction with two sets of topography equipment; a Rigaku and Jarrell-Ash. The x-ray tube was operated with a Mo target at 40 KV and 3.0 MA.

The topographs were recorded on Ilford L-4 nuclear plates with a 50μ emulsion thickness at exposures of about 1 1/2 hrs per mm of horizontal scan. The plates wore processed at 2°C in order to insure uniform development throughout the emulsion thickness. The plates were first held in water for 10 minutes then developed in a 2:1 mixture of water to D-19 for 20 minutes followed by 10 minutes in a stop bath. After fixing at room temperature for 1 hr, the plates were washed in running water for 3 hrs. The topographs were subsequently enlarged with an optical transmission microscope so that the resulting prints are actually negative prints.

The resolution of the x-ray topograph method depends on many factors. Assuming that the desired $K\alpha_1$ peak is separated from the $K\alpha_2$ peak, the following factors all influence the horizontal resolution;

(i) wave length spread of x-ray emission profile

(ii) intrinsic reflecting range of crystal

(iii) perpendicularity of emulsion to diffracted beam.

The effect of the first two factors on resolution depends on the specimen to emulsion distance which must therefore be kept as small as possible. The third depends on film alignment. When optimum conditions exist, the resolution resulting from these and other factors taken together is of the order of several microns. This resolution limit combined with the width of the dislocation image means that individual dislocations cannot be resolved for densities greater than about 5×10^5 dislocations per cm^2.

II. EXPERIMENTAL

A. Specimen Characteristics

1. Material

All the test specimens used in this study were cut from one single crystal which was 7 1/2 inches long and 1 1/2 inches in diameter as supplied by the Monsanto company. The growth direction was ⟨111⟩ and the resulting dislocation density was determined to be essentially zero. The crystal was boron doped (P type) which gave a resistivity that averaged 43 ohm-cm along the growth direction.

2. Specimen Size and Shape

The limited volume of available material coupled with the desirability of having a stress intensity that varied slowly with crack length predicated the use of crackline-loaded edge-crack specimen. Srawley and Gross[11] have done boundary collocation analyses on this type of fracture specimen and the design utilized in this study is based on their results. Figure 1 shows the specimen shape and size along with the variation of the stress intensity with crack length as tabulated by Srawley and Gross. The stress intensity for this specimen design is almost constant over a substantial fraction of the crack path.

The specimen thickness was determined by the optimum transmission conditions for primary extinction contrast. For silicon and Mo $K\alpha_1$ radiation the optimum thickness is 1 mm.

3. Crystallographic Orientation

Figure 2 illustrates the relationship between the crystallographic directions and the plane of maximum tensile stress. The stress fracture plane thus coincides with a {111} plane which is the preferred plane for fracture in silicon. The remaining three {111} planes are oriented

so as to provide a plastic zone at the crack tip which is symmetric with respect to the fracture path.

The accuracy of the specimen crystallographic alignment as checked by back reflection Laue analysis was always within several degrees of the desired orientation.

4. Machining and Surface Finishing

The specimens were cut to the desired shape from the single crystal and notched with lubricated diamond saws mounted on a goniometer equipped cut-off machine. The loading-pin holes were diamond drilled.

The machining abrasions were removed by chemically polishing away at least 25μ from the surface. The chemical polish used was as follows; A fresh mixture of 65% A and 35% B where (A) is a 3:1 mixture of HNO_3 and 48% HF and (B) is 2.5 gm. of iodine in 1100 ml. of glacial acetic acid.

B. Testing Procedures

1. Precracking

Mathematically sharp cracks were introduced completely elastically into the fracture specimens at the root of the machined notch and lying in the fracture plane via the following technique. After chemically polishing the surface, the notch root was scratched with a tungsten carbide stylus. Subsequently, a 10° alumina wedge was slowly forced into the notch with the Instron machine while a constant compressive load was applied perpendicularly to the fracture plane further down the crack path. The compressive loading device is shown in Fig (3). The spring-loaded arrangement was calibrated so that a known compressive force could be applied. Any crack propagating down the fracture plane would experience a transition from tensile to compressive loading and thus be

I. INTRODUCTION

The purpose of this study was to examine in detail the plasticity and fracture characteristics of sharp cracks in a crystalline material. The intent was to utilize the simplest experimental situation possible so that a minimum of physical parameters would be involved. In this regard the most appropriate material would be single crystalline, defect free, reasonably elastically isotropic and with a crystal structure whose plasticity characteristics are easily analysed. Further, the specimen design would be such that the theories of fracture mechanics, especially those associated with mathematically sharp cracks under mode I loading conditions, could be employed in conjunction with the dislocation theories of plasticity.

Single crystalline silicon was chosen for this investigation for several reasons. From the practical point of view, large defect-free single crystals are readily and inexpensively available commercially as a result of research in the semiconductor industry. The more scientific advantages are that the diamond cubic crystal structure exhibits dislocation glide systems that are analogous to the face centered cubic crystal structure [1] as well as being reasonably elastically isotropic.[1] The primary difference between silicon and most FCC metals is that plasticity in silicon is strongly rate dependent and occurs in appreciable quantities only above about 600°C.[2,3] This latter characteristic may be exploited by "freezing-in" at room temperature the dislocation configurations obtained at high temperatures or, conversely, by producing dislocation-free cracks at room temperature for subsequent testing in the range of plasticity. Finally, silicon is particularly amenable to examination via x-ray topography[4] because of the low mass

absorption coeffieient. This allows a specimen thickness that is suitable for mechanical testing as well as for non-destructive observation with x-ray topography. X-ray topography was used extensively in this study to determine the extent and nature of dislocation configurations because of this advantage.

Previous work associated with the topic of this study has been done on Fe-3% Si,[5,6] LiF[7], MgO[8] and Zn[9]. It appears however that only one cursory study[10] on Si at elevated temperatures has involved fracture. In all of the above cases some of the pertinent experimental parameters such as applied load, deflection rate, stress intensity and initial mobile dislocation density were unknown. The studies that most resemble the scope of this thesis were performed on LiF with pinned dislocations. The nature of the plasticity however was determined by etch pit analysis which does not verify the operative burger's vector. This study intended to further the knowledge of interactions between crack stress fields and plasticity mechanisms in the case where all the dislocations are produced by the crack tip. The dislocation configurations thus produced were to be characterized explicitly via x-ray topography.

THEORETICAL AND EXPERIMENTAL STUDIES OF FLOW AND FRACTURE IN MONOCRYSTALLINE SILICON

Charles Falding St. John

Inorganic Materials Research Division, Lawrence Berkeley Laboratory and Department of Materials Science and Engineering, College of Engineering; University of California, Berkeley, California

ABSTRACT

The flow and fracture associated with sharp cracks under mode I loading in monocrystalline silicon has been studied under varying conditions of loading rate and temperature. Sharp cracks were introduced completely elastically at room temperature with an apparatus designed to position appropriately the crack plane and tip with the specimen morphology and crystallography. The dislocation configurations produced from the crack tip in the temperature range of 700-950°C were examined in detail with an x-ray topographical technique. Room temperature tests were conducted to determine the effective crack surface energy and also to verify the theoretical variation of stress intensity with crack length for the particular crackline-loaded edge-crack specimen design utilized in this study.

The brittle to ductile transition temperature range for sharp-cracked specimens was found to be extremely narrow, of the order of several degrees centigrade. Further, the rate dependency of the transition temperature range obeyed an activation energy of 1.9 eV which compares well with the activation energy for dislocation glide in silicon as established elsewhere from dislocation velocity studies on material of similar purity and defect density. A relationship was developed that showed that the brittle to ductile transition temperature is dependent on the rate of enlargement of the crack tip radius and hence related to dislocation motion.

Relationships for the force fields exerted on each of the twelve glide systems emanating from the crack tip were calculated from the continuum mechanical theories for stress fields at sharp cracks and the crystallographic relationship between the crack and specimen crystallography. The favored glide systems could be thereby predicted for each slip plane under conditions of either plane strain or plane stress. A detailed study of many crack tip plastic regions with x-ray topography showed that the operative glide systems were the same as those predicted by theory.

A room temperature surface energy for silicon of 2700-2800 ergs/cm^2 was obtained from the results of eight specimens, where each specimen averaged four to five fractures. The results of crack extension and arrest were analysed from both stress intensity and strain energy release rate approaches and good agreement was obtained between the two types of analyses. No reason was established for the apparently high surface energy found in this study as compared to the results of another investigation which utilized similar techniques.

Successive fracturing in the room temperature specimens allowed the experimental verification of the theoretical variation of stress intensity with crack length as obtained from boundary collocation.

THEORETICAL AND EXPERIMENTAL STUDIES OF FLOW AND FRACTURE IN MONOCRYSTALLINE SILICON

Contents

Abstract v

I. Introduction 1

II. Experimental

A. Specimens Characteristics 3

1. Material 3

2. Specimen Size and Shape 3

3. Crystallographic Orientation 3

4. Machine and Surface Finishing 4

B. Test Procedures 4

1. Precracking 4

2. Fracture Testing 5

C. X-ray Topography 5

III. Results and Discussion

A. Precracking 7

B. Room Temperature Tests 8

1. Stress Intensity Approach 8

2. Strain Energy Release Rate Approach 10

3. Fracture Surface Morphology 12

4. Other Surface Energy Considerations 14

C. High Temperature Results 17

1. Brittle to Ductile Transition 17

2. Dislocation Configurations at the Crack Tip 23

IV. Conclusions 33

Acknowledgements 34

Appendix 35

References 38

Figure Captions 40

Figures 43

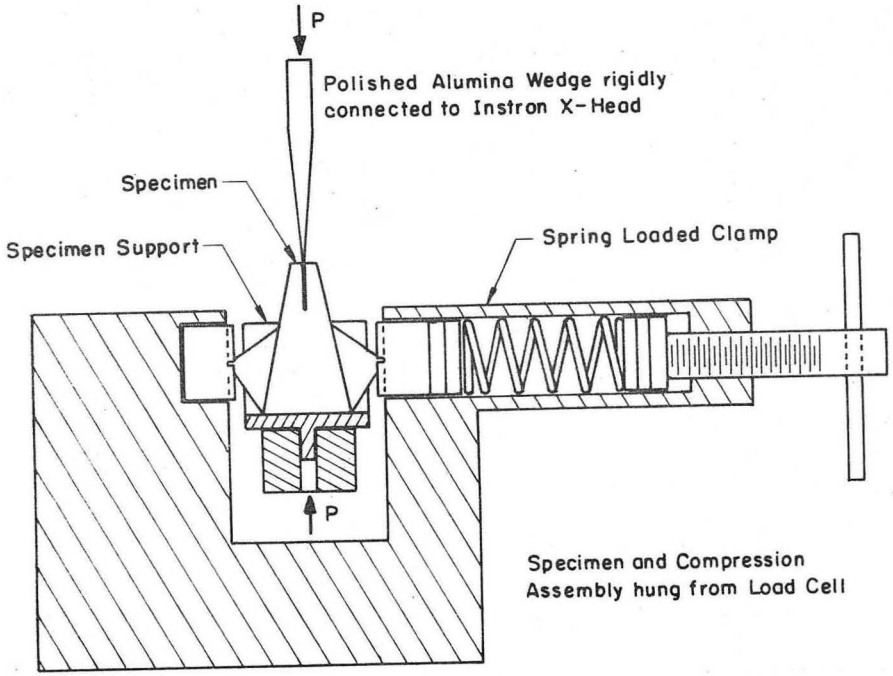

XBL 718-7099

Fig. 3

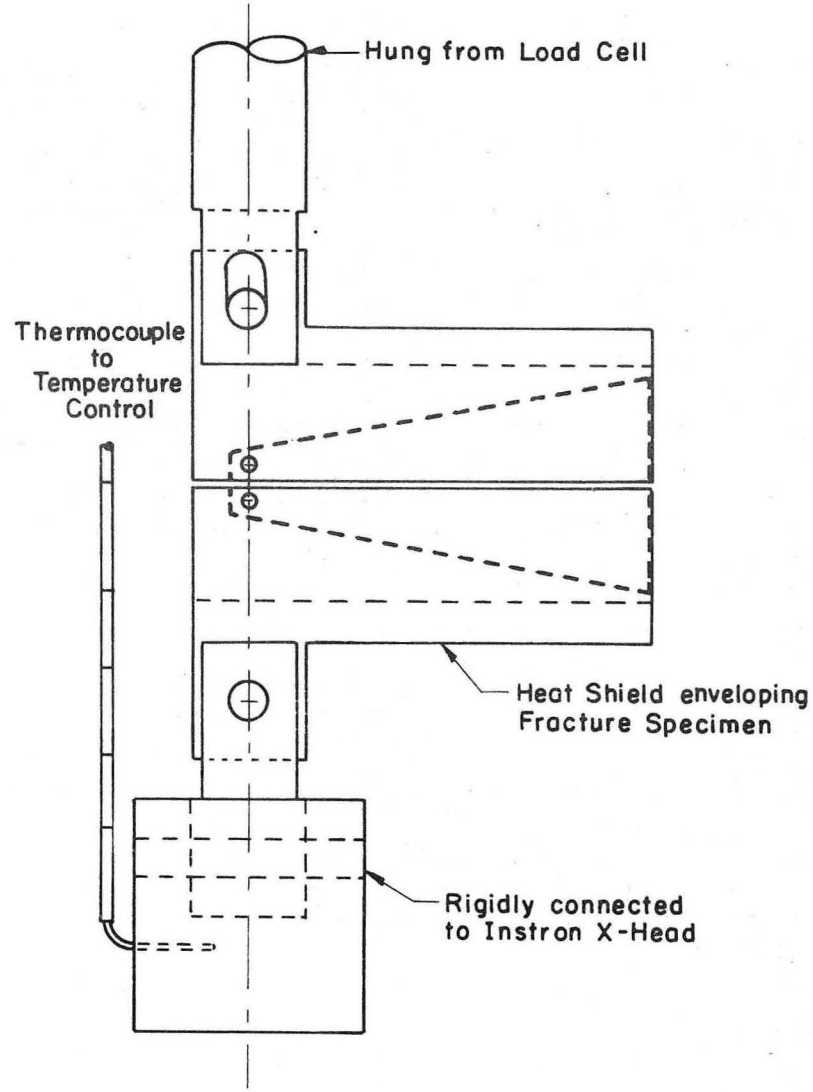

XBL 718-7100

Fig. 4

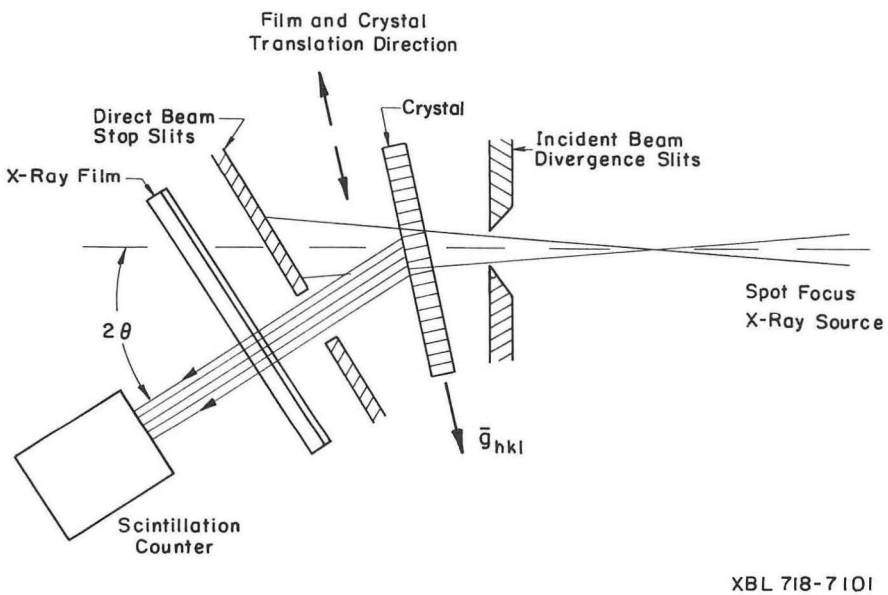
Film and Crystal
Translation Direction
Direct Beam
Stop Slits
Crystal
Incident Beam
Divergence Slits
X-Ray Film
Spot Focus
X-Ray Source
2θ
$\bar{g}_{hkl}$
Scintillation
Counter
XBL 718-7101

Fig. 5

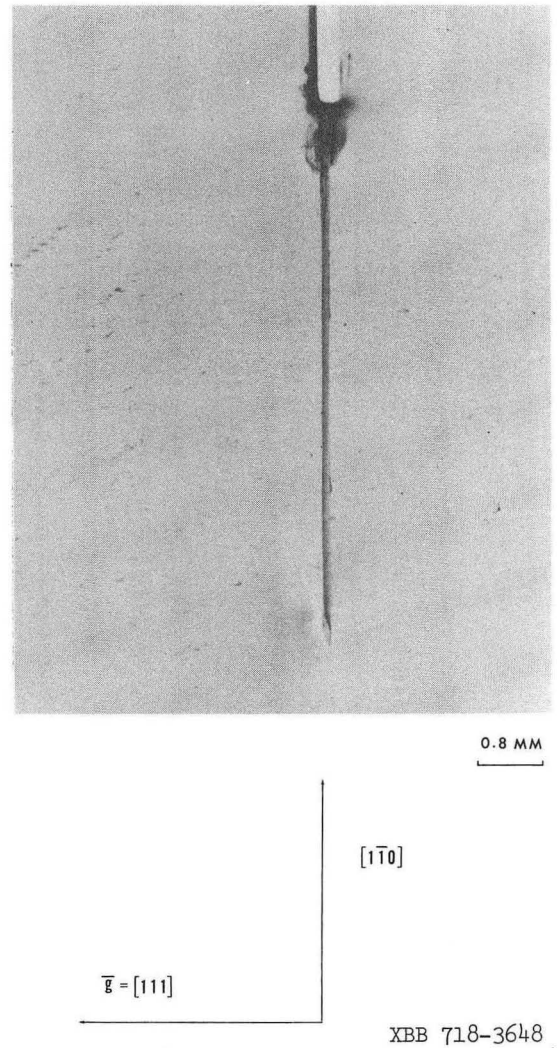
0.8 MM
[1$\bar{1}$0]
$\bar{g}$ = [111]
XBB 718-3648

Fig. 6

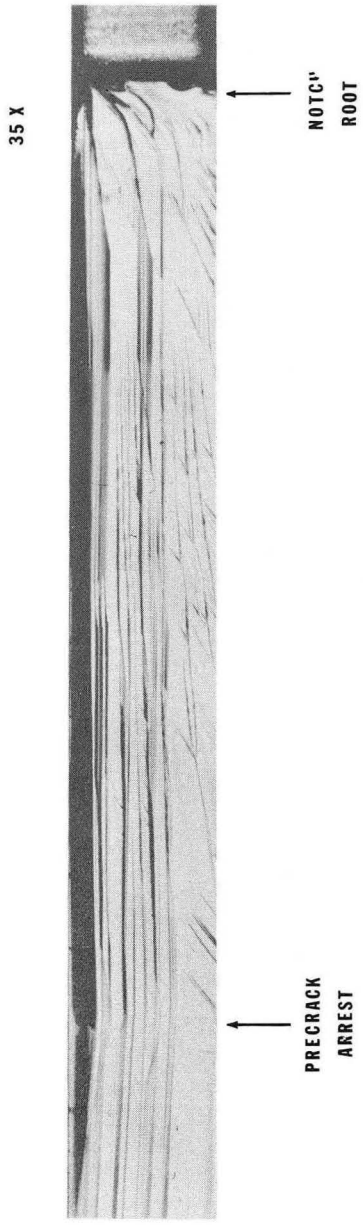

XBB 718-3647

Fig. 7

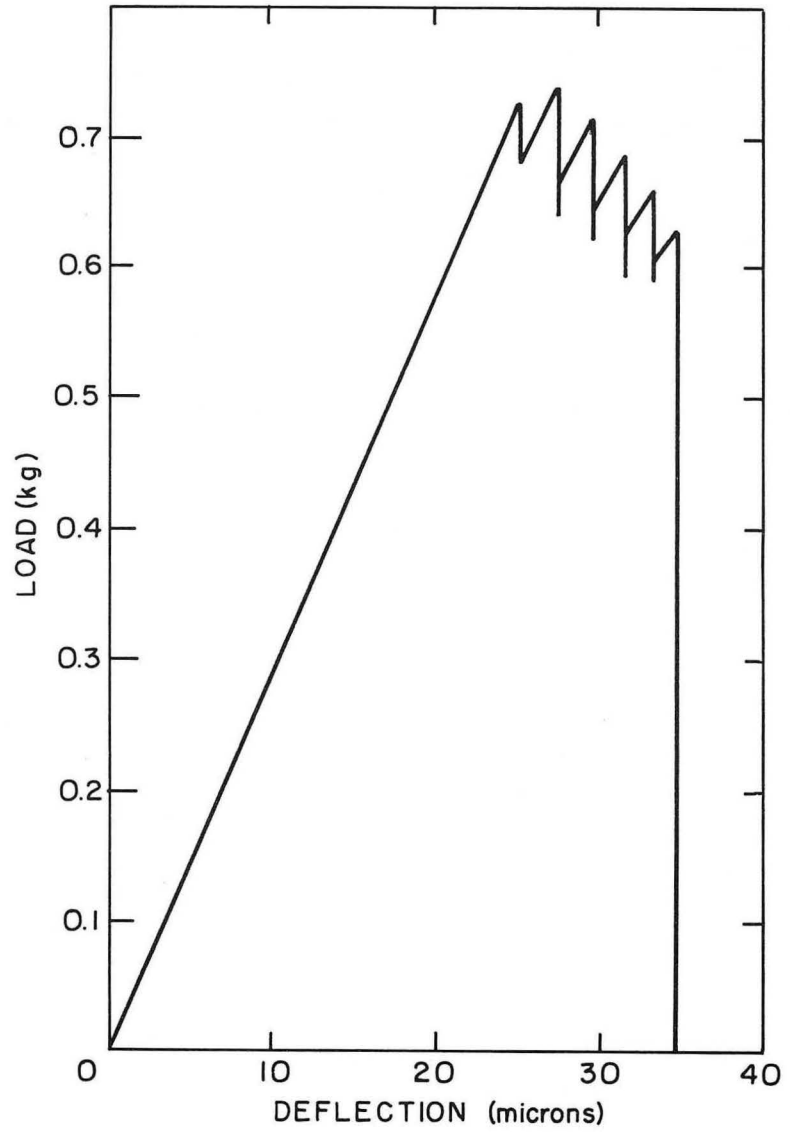

XBL718-7102

0 0 0 0 3 6 0 0 7 7 3

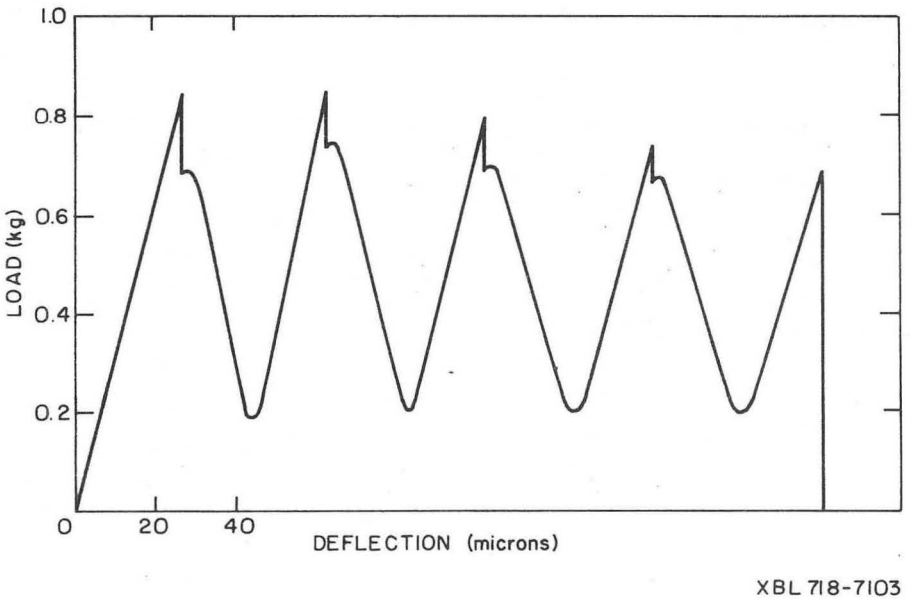
1.0
0.8
0.6
0.4
0.2
LOAD (kg)
0
20
40
DEFLECTION (microns)
XBL 718-7103

Fig. 9

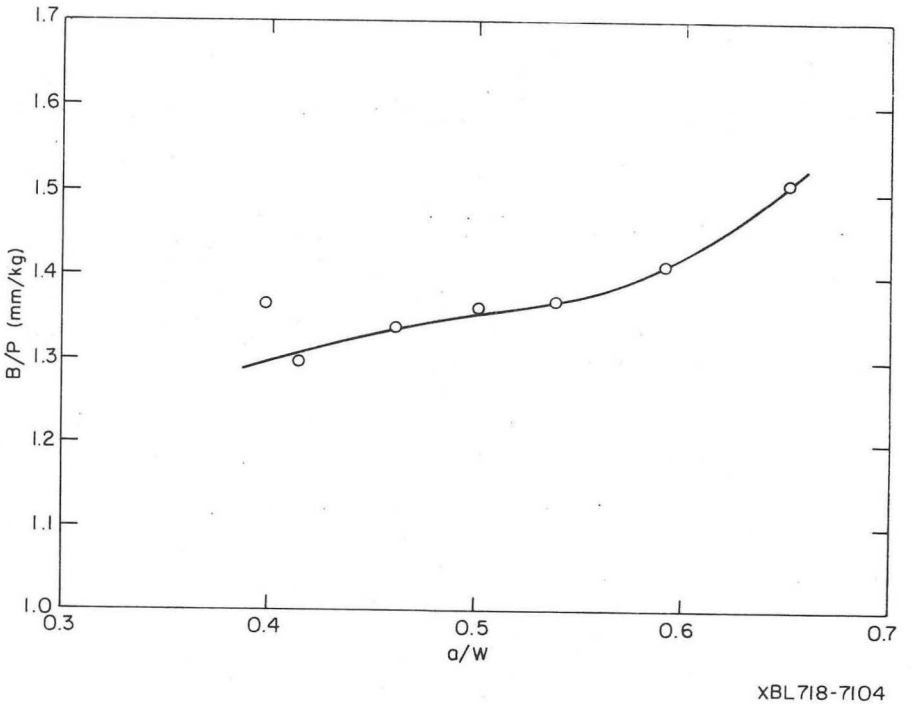
1.7
1.6
1.5
1.4
1.3
1.2
1.1
1.0
B/P (mm/kg)
0.3
0.4
0.5
0.6
0.7
a/W
XBL718-7104

Fig. 10

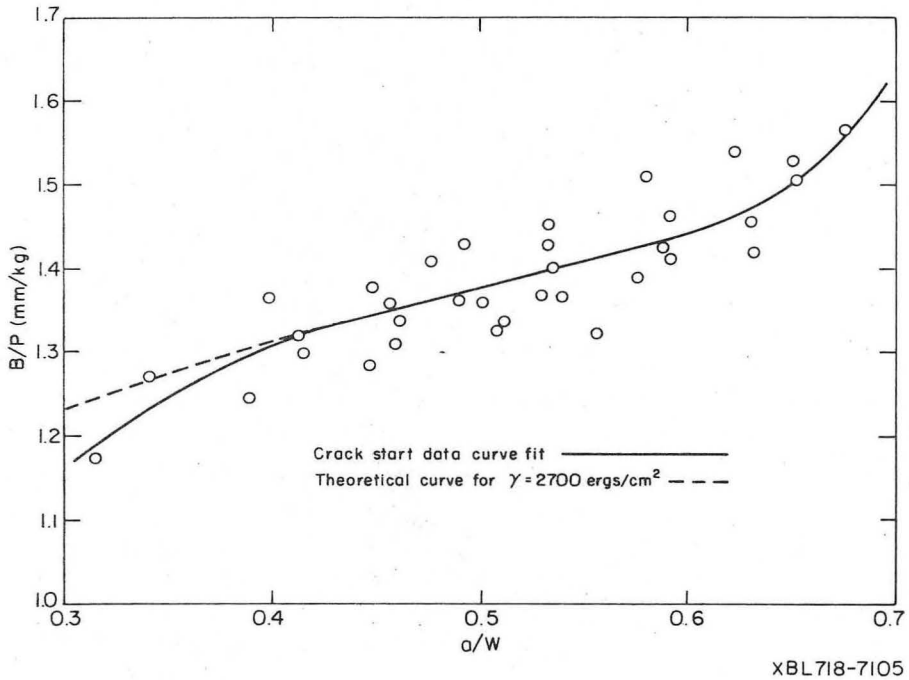
1.7
1.6
1.5
1.4
1.3
1.2
1.1
1.0
B/P (mm/kg)
0.3
0.4
0.5
0.6
0.7
a/W
Crack start data curve fit
Theoretical curve for $\gamma = 2700$ ergs/cm^2
XBL718-7105

Fig. 11

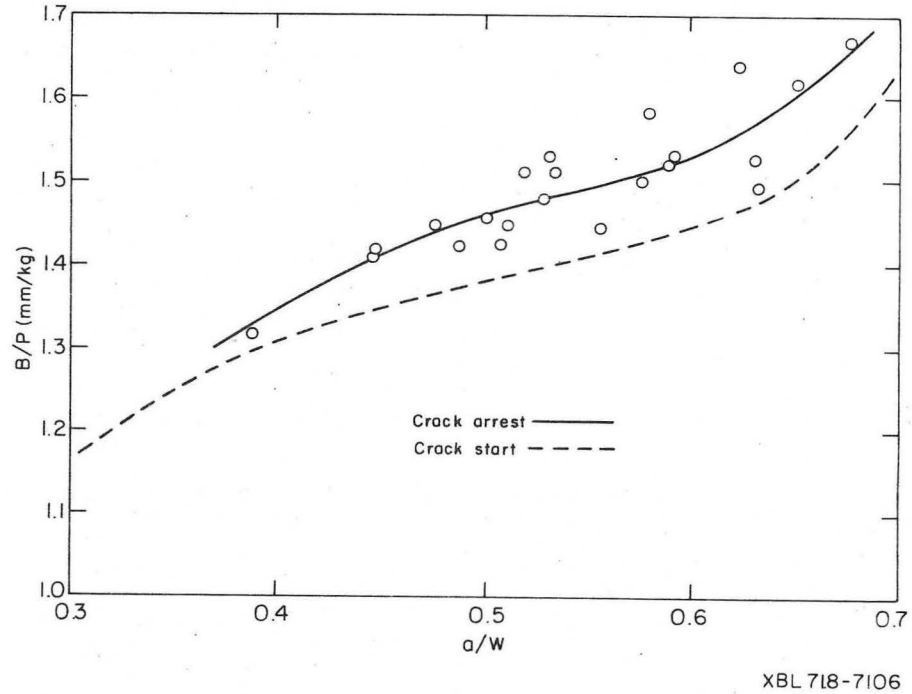
1.7
1.6
1.5
1.4
1.3
1.2
1.1
1.0
B/P (mm/kg)
0.3
0.4
0.5
0.6
0.7
a/W
Crack arrest
Crack start
XBL 718-7106

Fig. 12

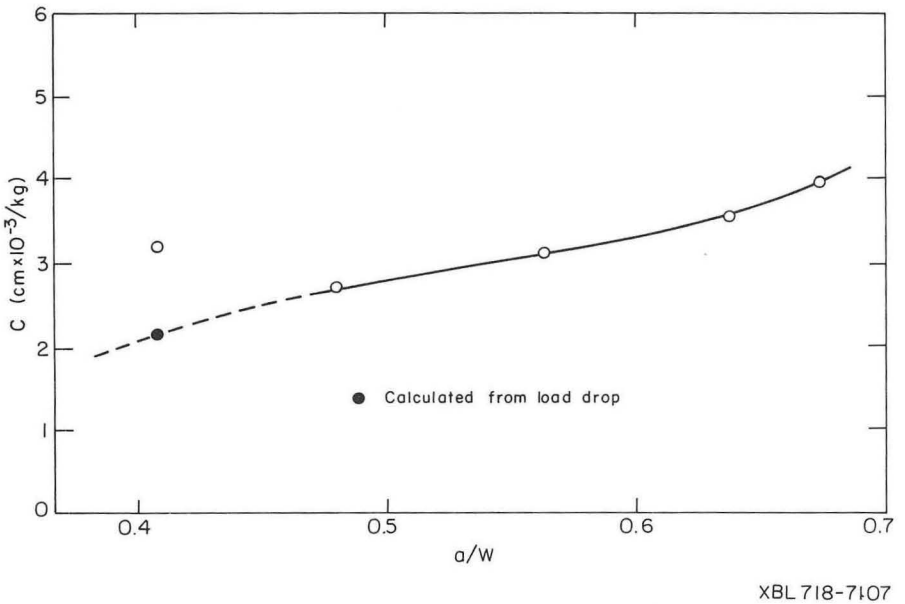
C (cm x10^{-3}/kg)
0
1
2
3
4
5
6
0.4
0.5
0.6
0.7
a/W
Calculated from load drop
XBL 718-7107

Fig. 13

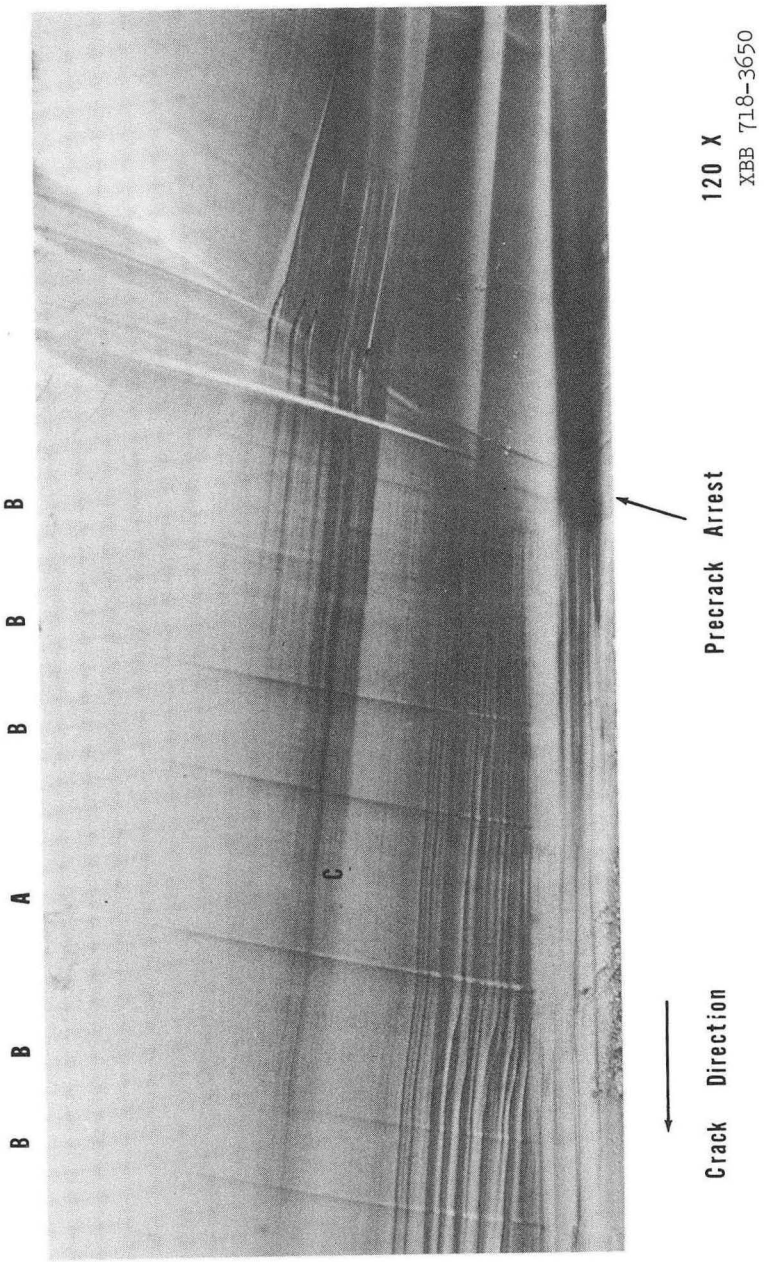
B
B
A
B
B
B
C
Crack Direction
Precrack Arrest
120 X
XBB 718-3650

Fig. 14

CRACK DIRECTION

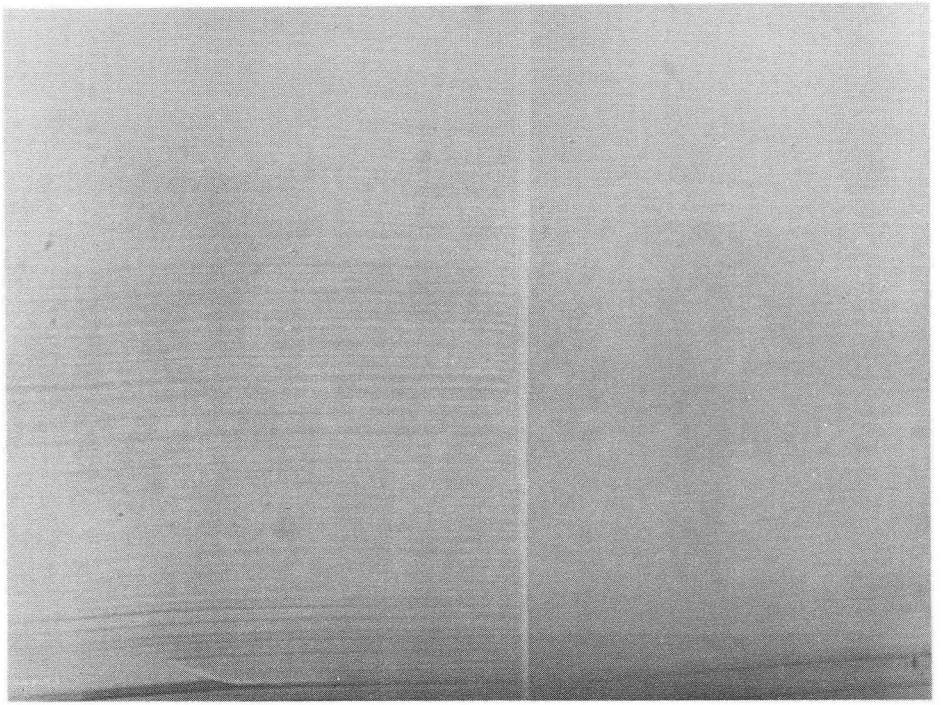

0.05 mm

XBB 718-3651

Fig. 15

CRACK DIRECTION

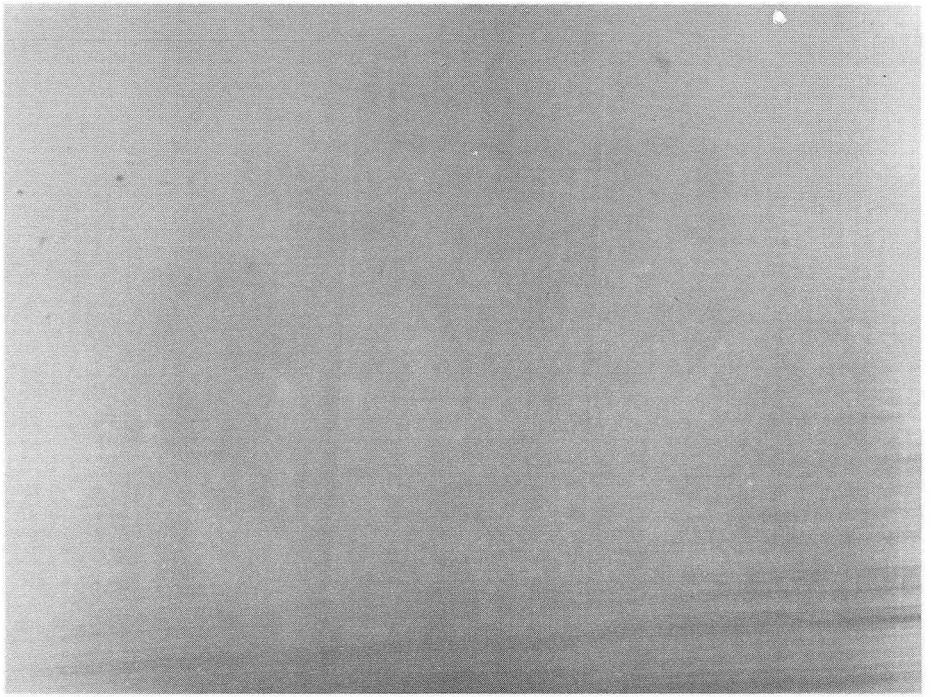

0.05 mm

XBB 718-3652

Fig. 16

0 0 0 0 3 6 0 0 7 7 5

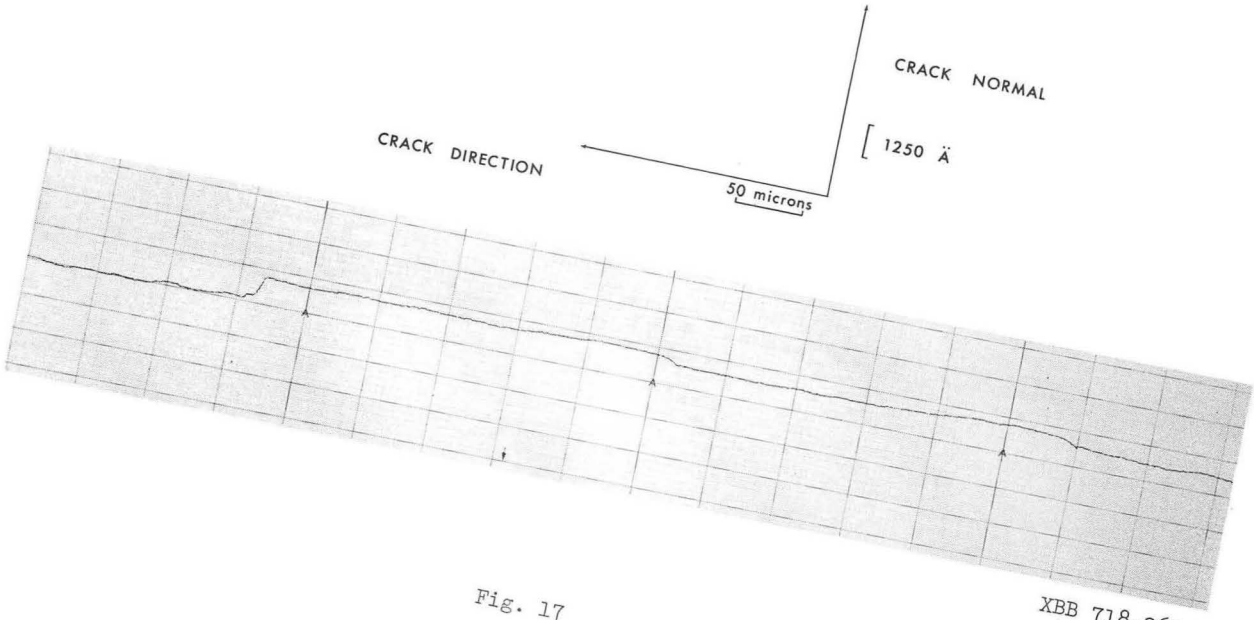

Fig. 17

XBB 718-3653

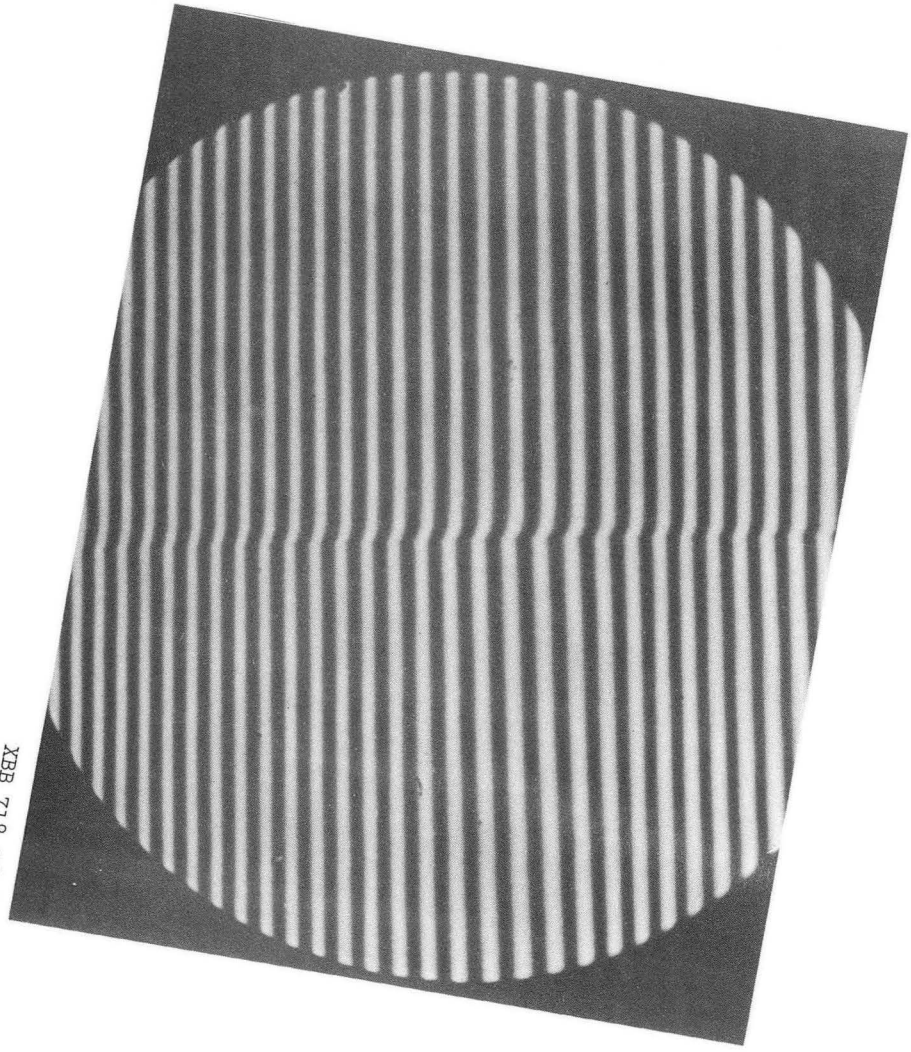

Fig. 18

XBB 718-3656

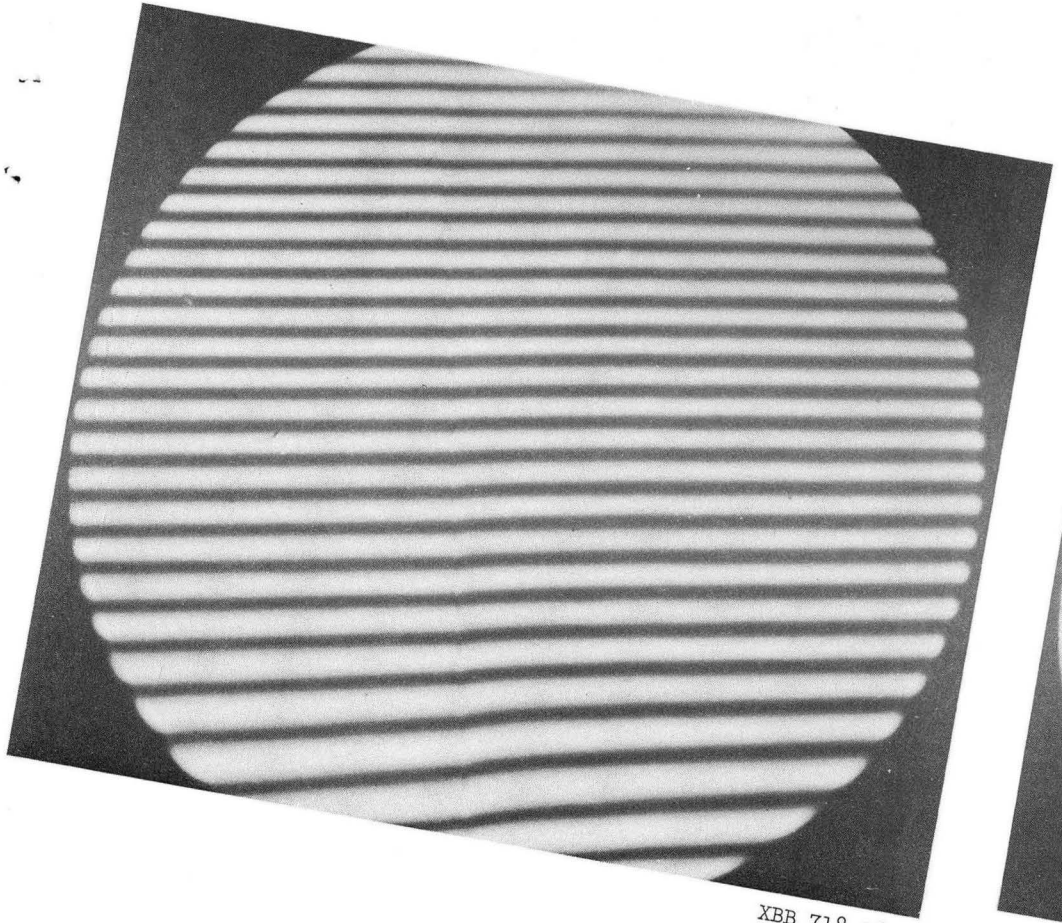

XBB 718-3655

Fig. 19

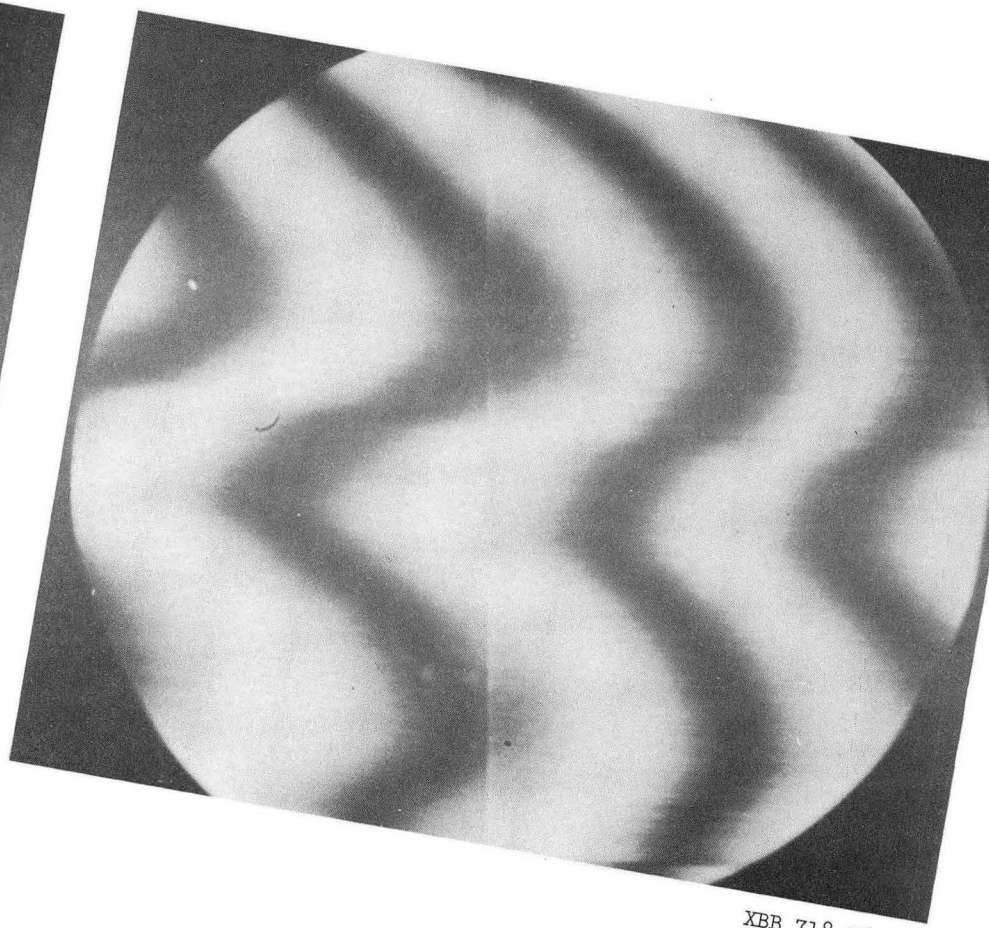

XBB 718-3654

Fig. 20

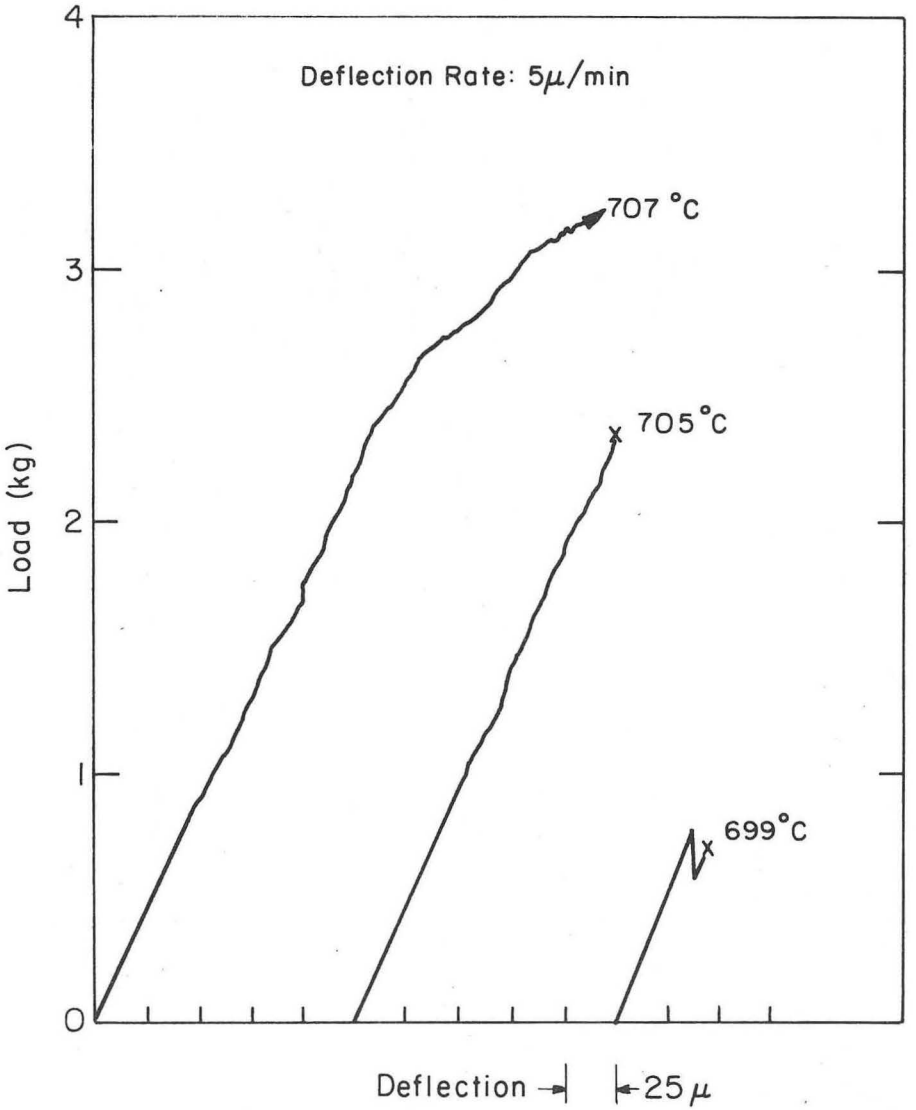

XBL 718-7108

Fig. 21

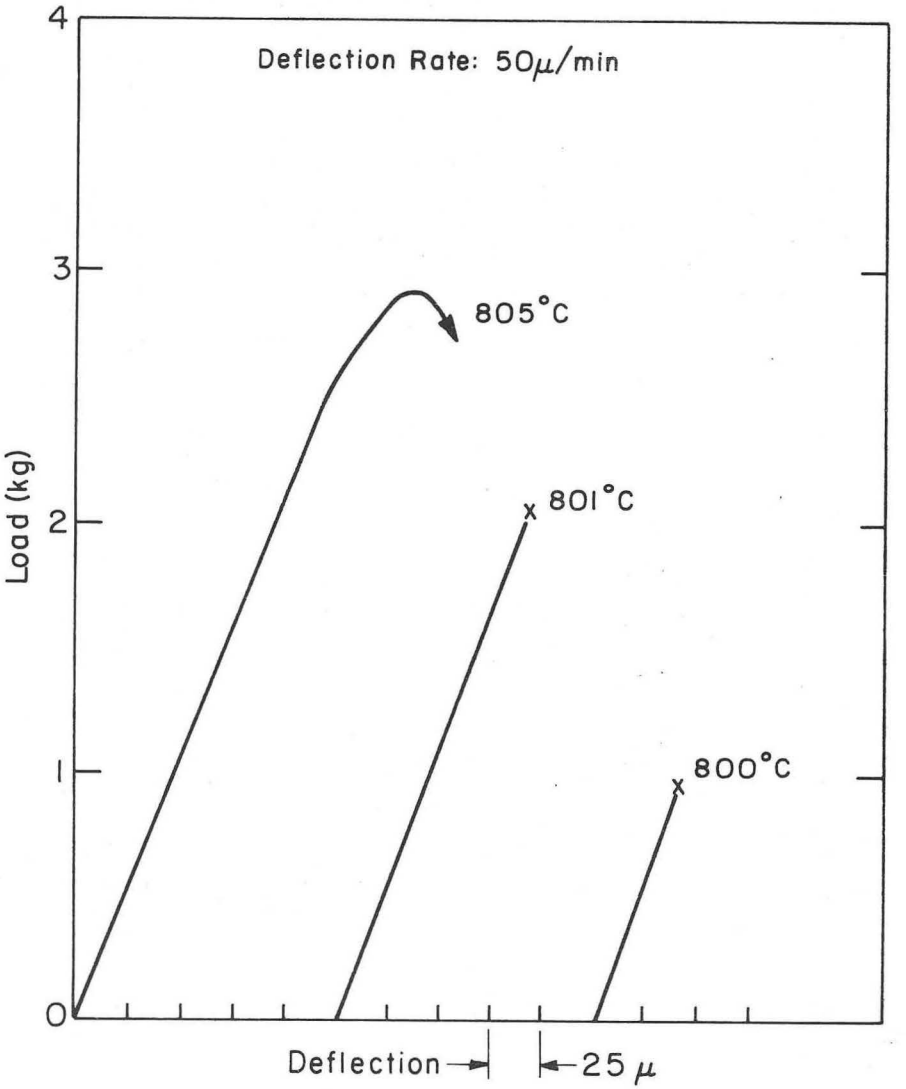

XBL 718-7109

Fig. 22

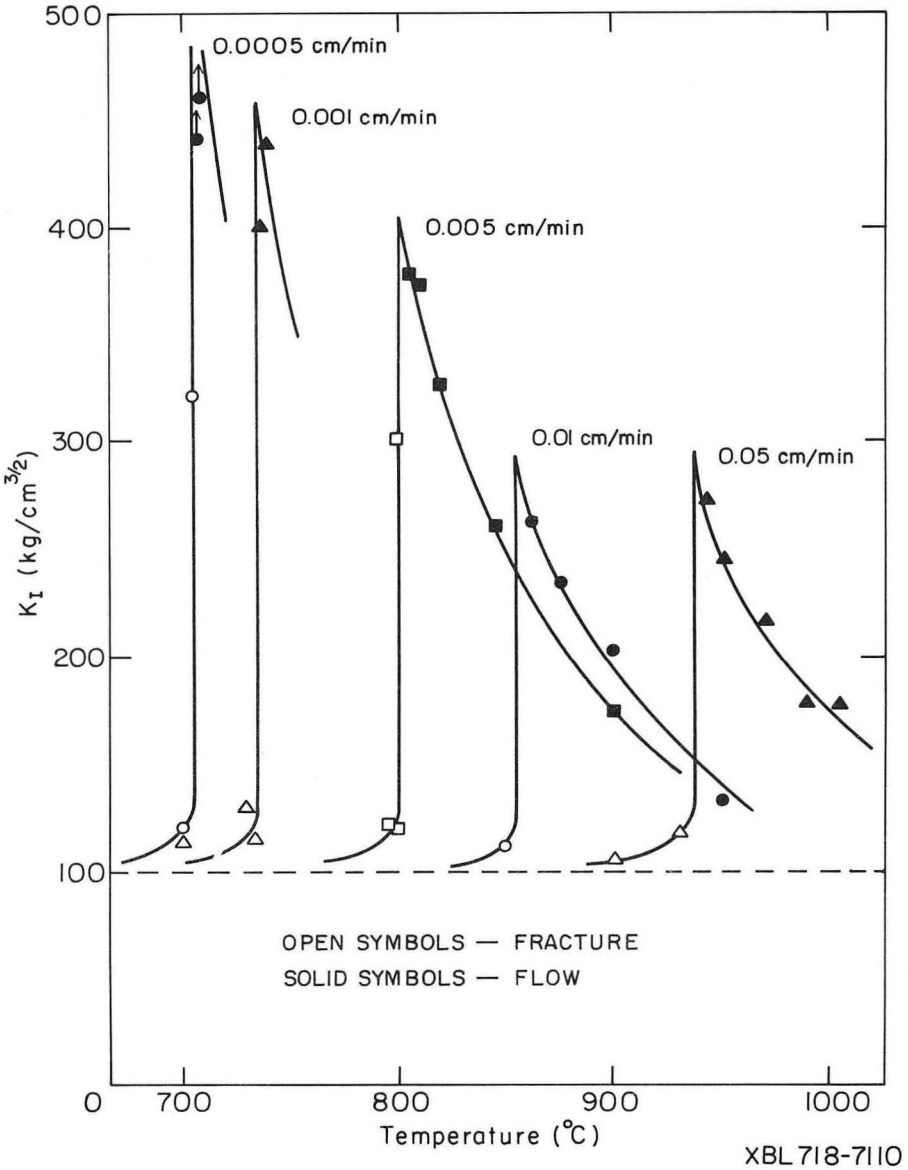

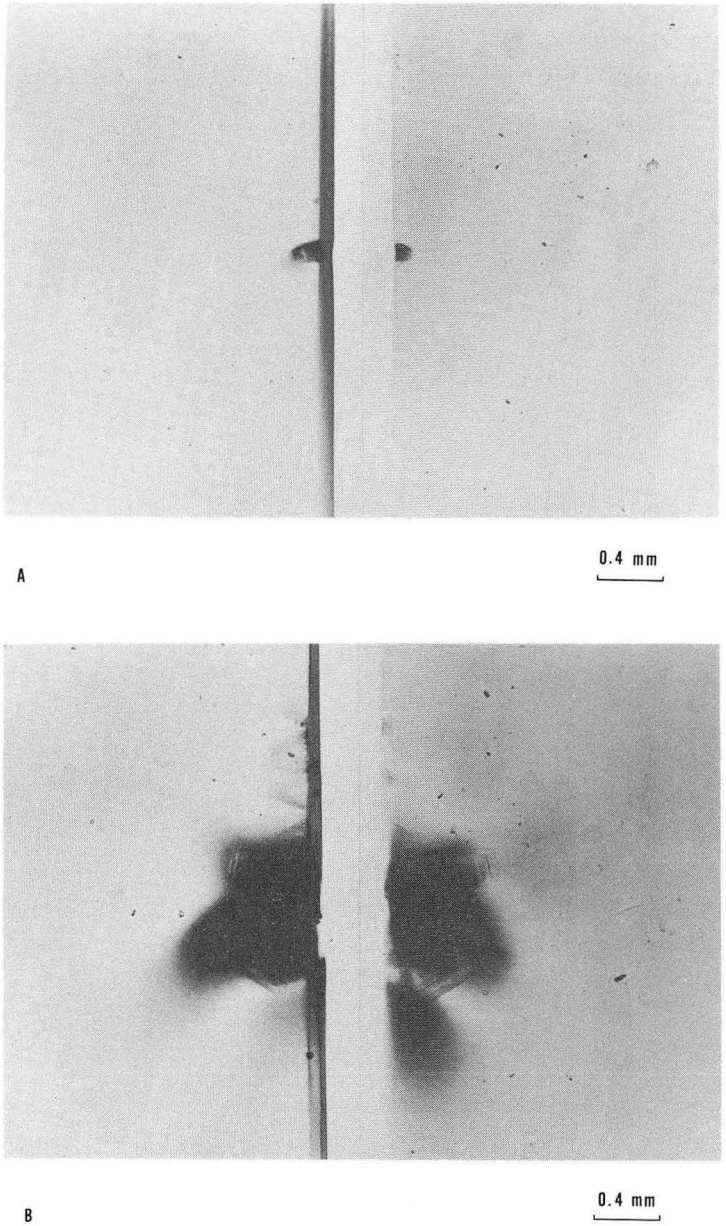

XBB 718-3643

Fig. 24

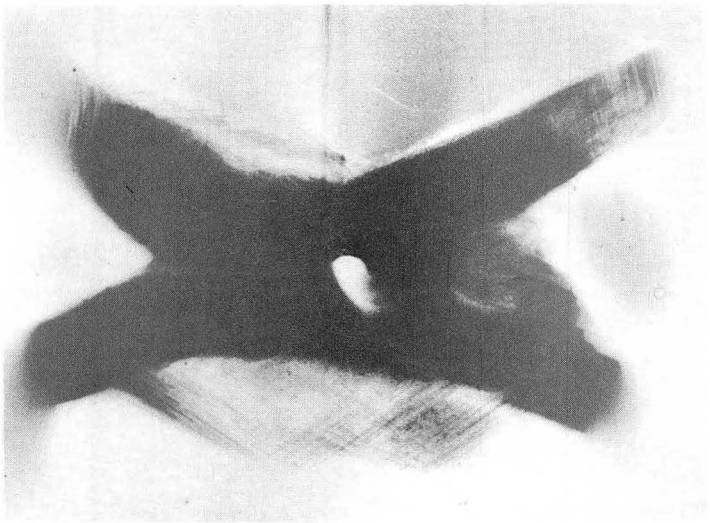

C

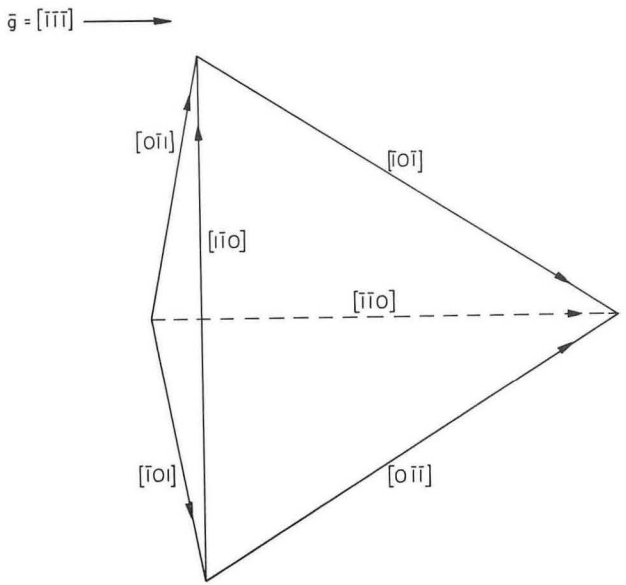

XBB 718-3642

Fig. 24

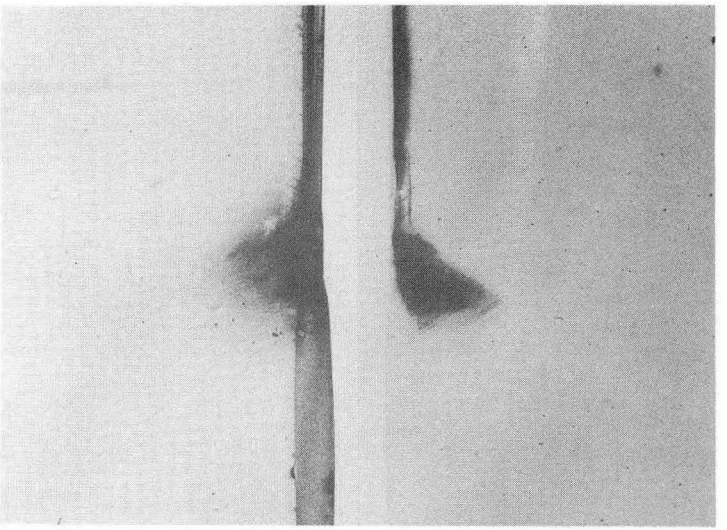

A

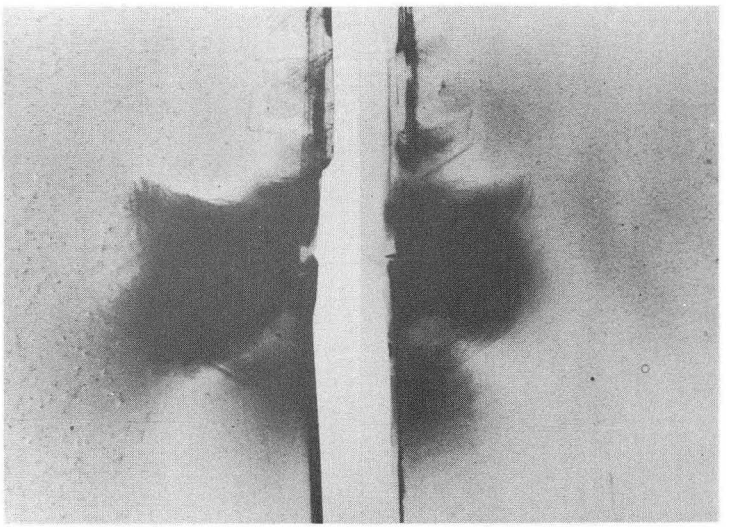

B

XBB 718-3646

Fig. 25

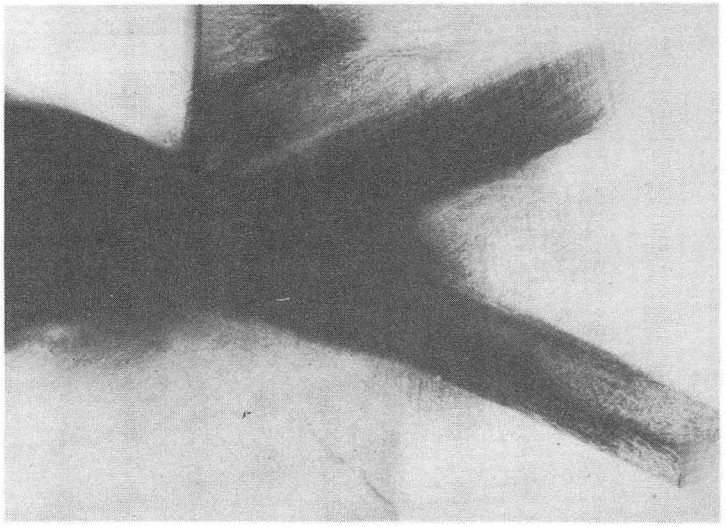

c

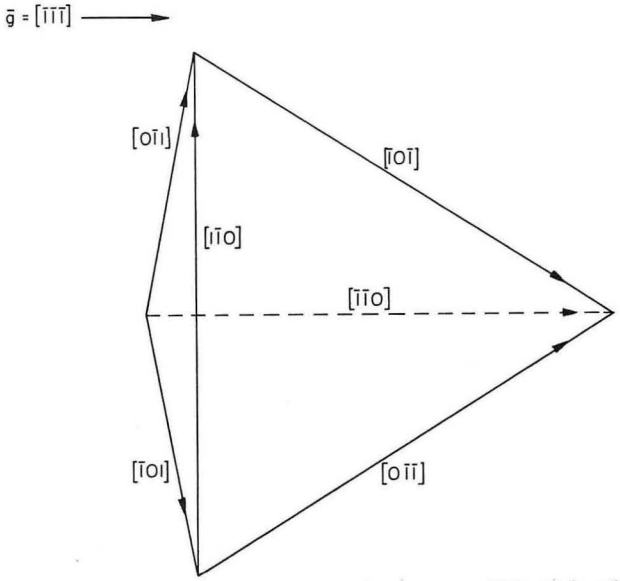

XBB 718-3640

Fig. 25

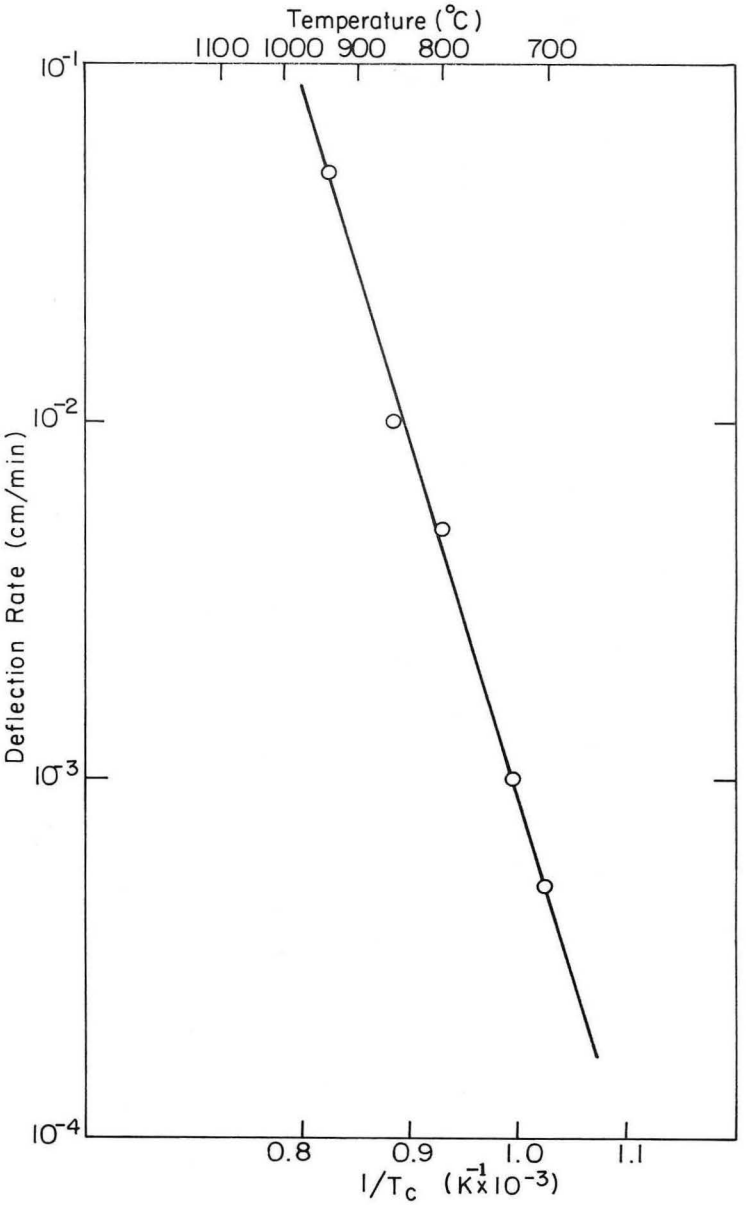

XBL 718-7111

Fig. 26

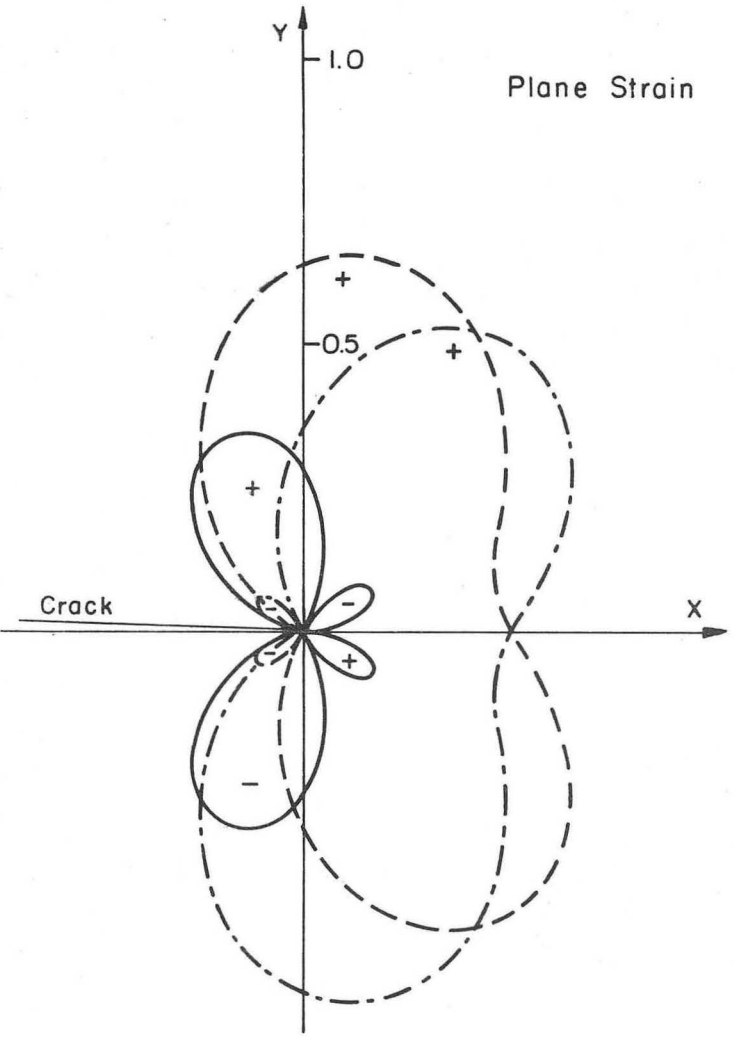

Glide Plane	Burgers Vector	Symbol
$(\bar{1}\bar{1}1)$	$[\bar{1}0\bar{1}]$	—·—
	$[0\bar{1}\bar{1}]$	— — —
	$[1\bar{1}0]$	———

XBL 718-7112

Fig. 27

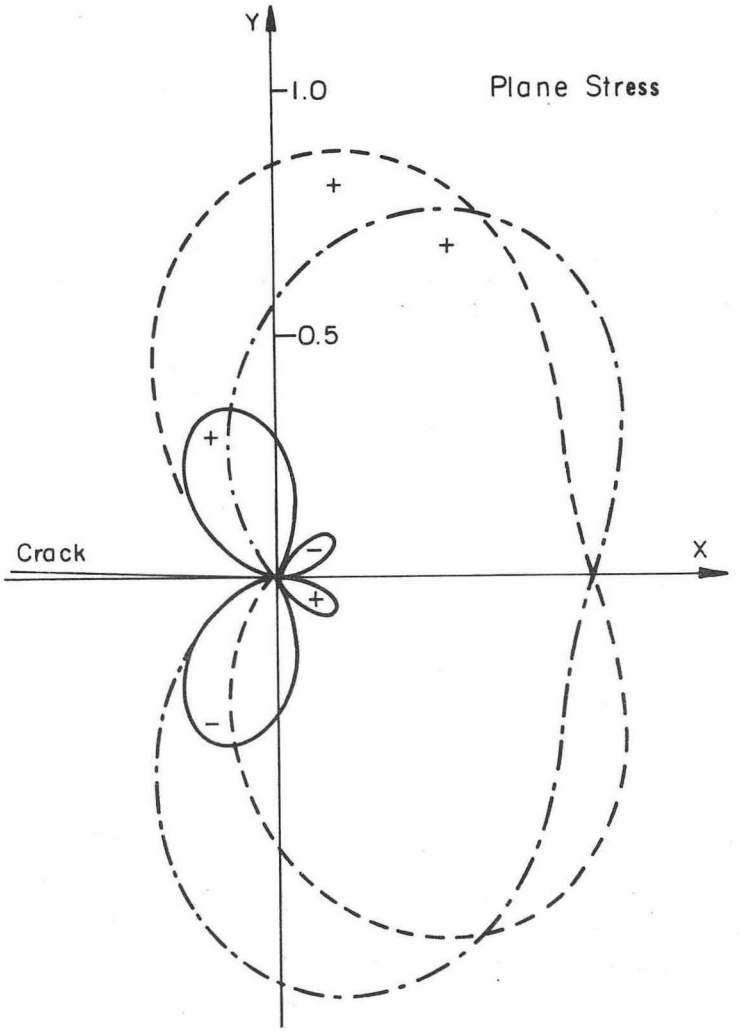

Glide Plane	Burgers Vector	Symbol
$(\bar{1}\bar{1}1)$	$[\bar{1}0\bar{1}]$	—·—
	$[0\bar{1}\bar{1}]$	— — —
	$[1\bar{1}0]$	———

XBL 718-7113

Fig. 28

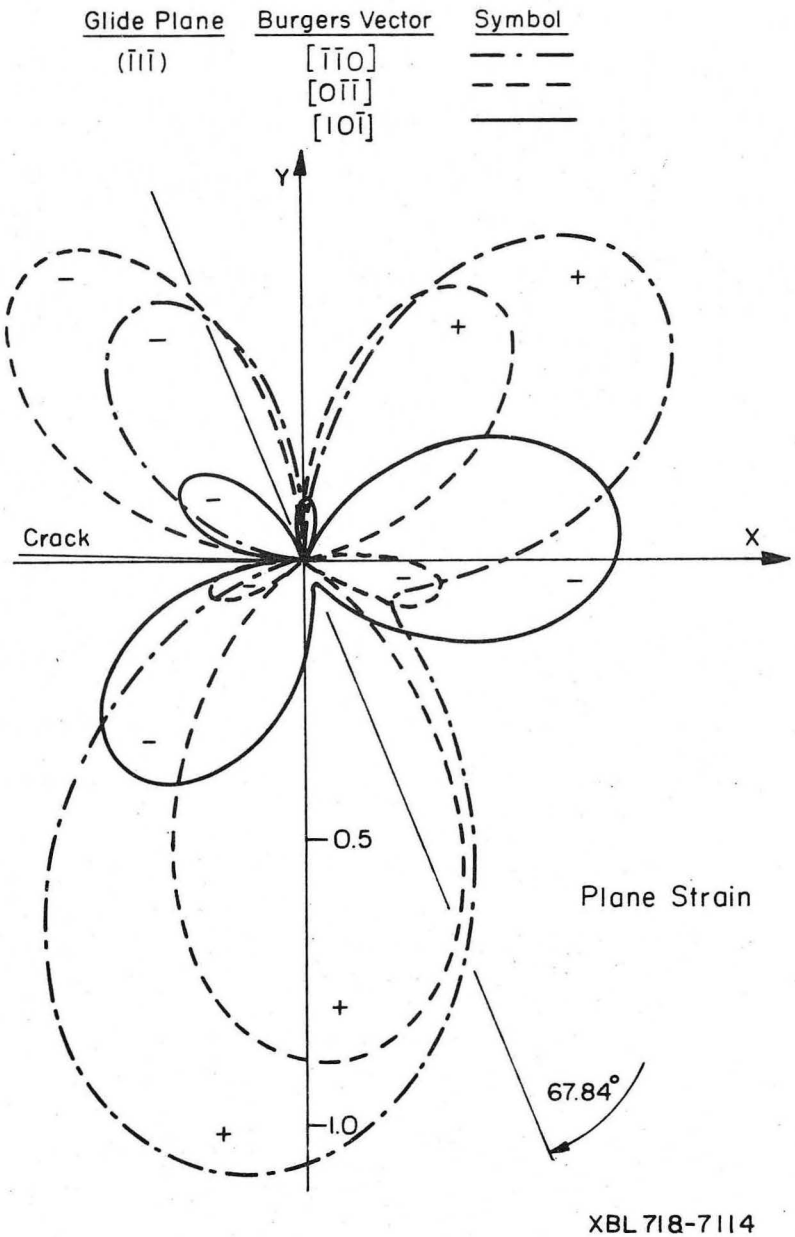
Glide Plane
Burgers Vector
Symbol
(1̄11̄)
[1̄1̄0]
[011̄]
[101̄]
Y
X
Crack
0.5
1.0
67.84°
Plane Strain
XBL 718-7114

Fig. 29

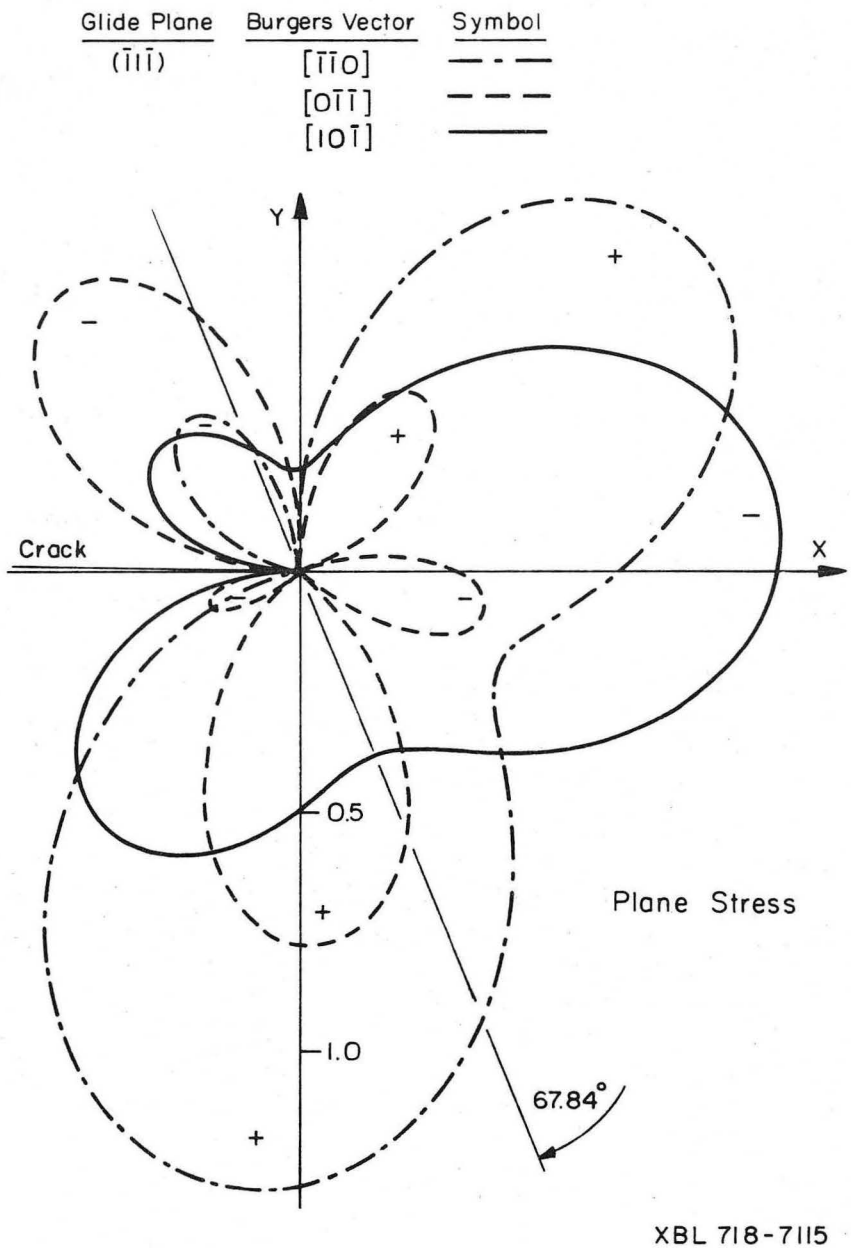
Glide Plane
Burgers Vector
Symbol
(1̄11̄)
[1̄1̄0]
[011̄]
[101̄]
Y
X
Crack
0.5
1.0
67.84°
Plane Stress
XBL 718-7115

Fig. 30

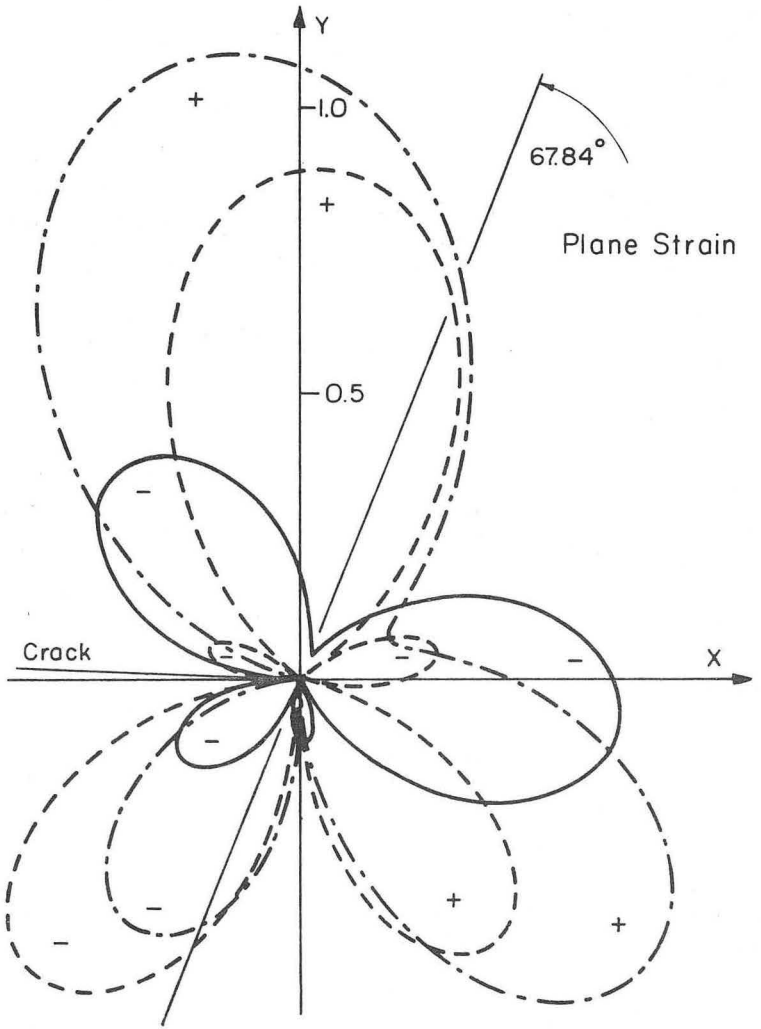

XBL718-7116

Fig. 31

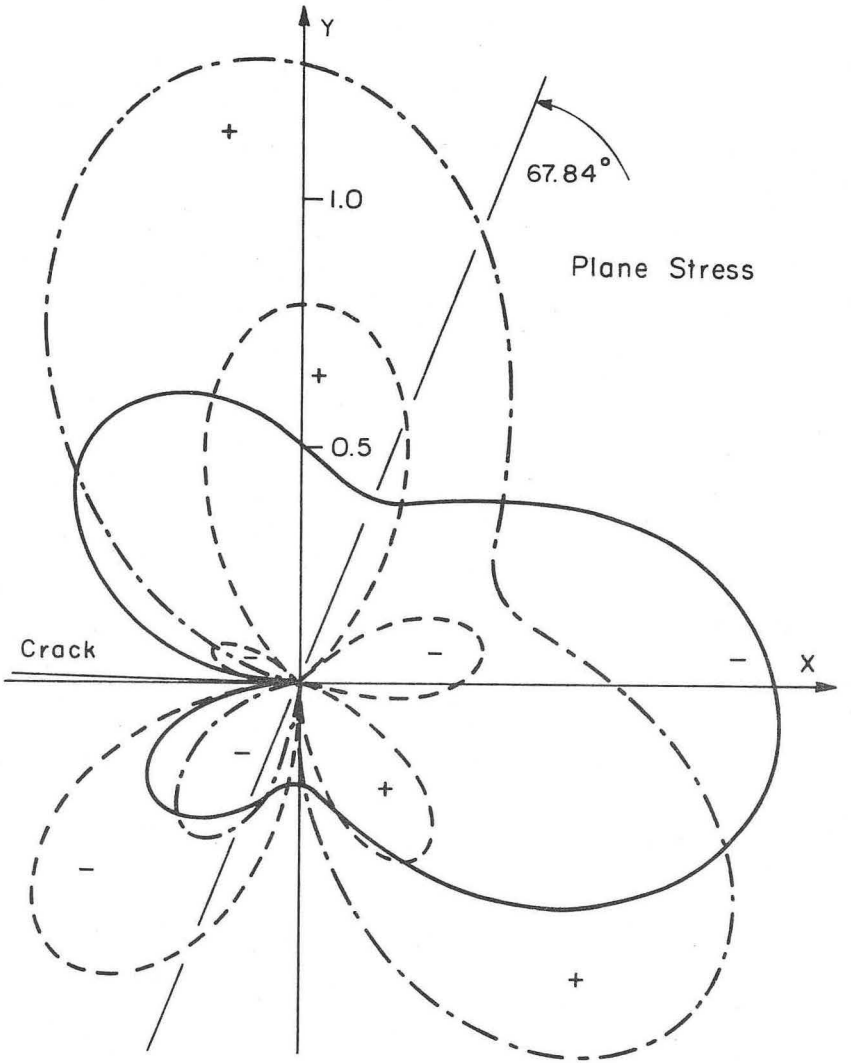

XBL718-7117

Fig. 32

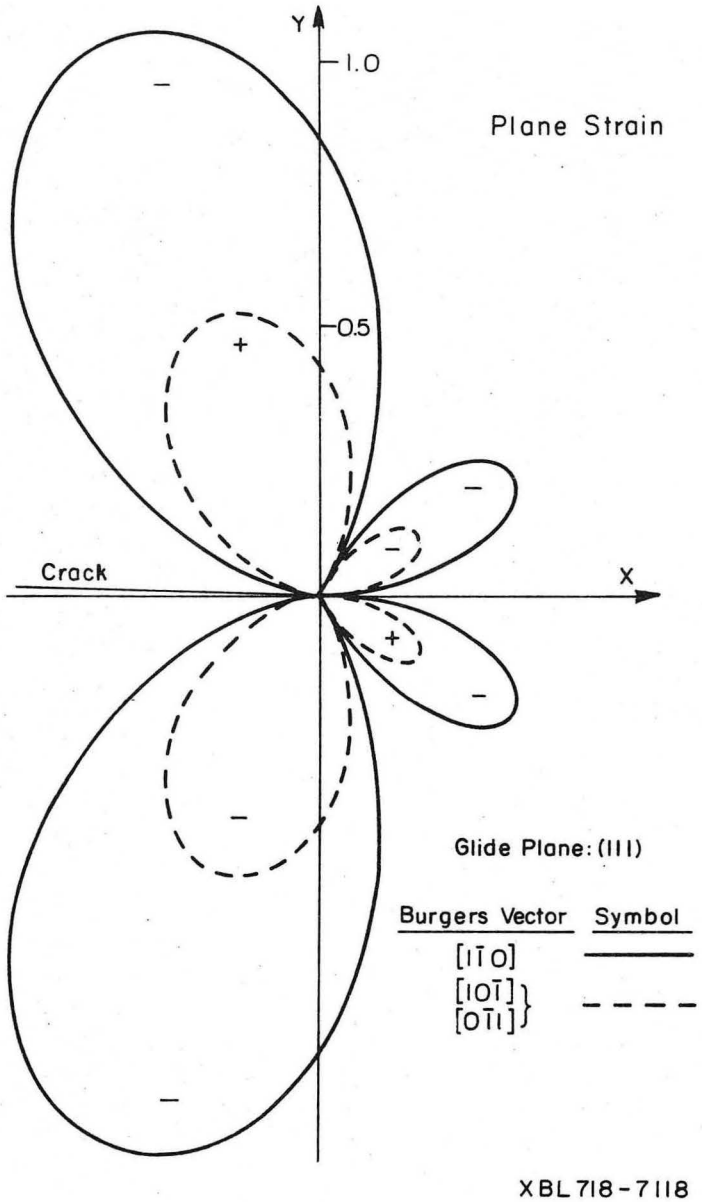
Y
1.0
0.5
Plane Strain
Crack
X
Glide Plane: (111)
Burgers Vector
Symbol
[1$\bar{1}$0]
[10$\bar{1}$]
[0$\bar{1}$1]
XBL718-7118

Fig. 33

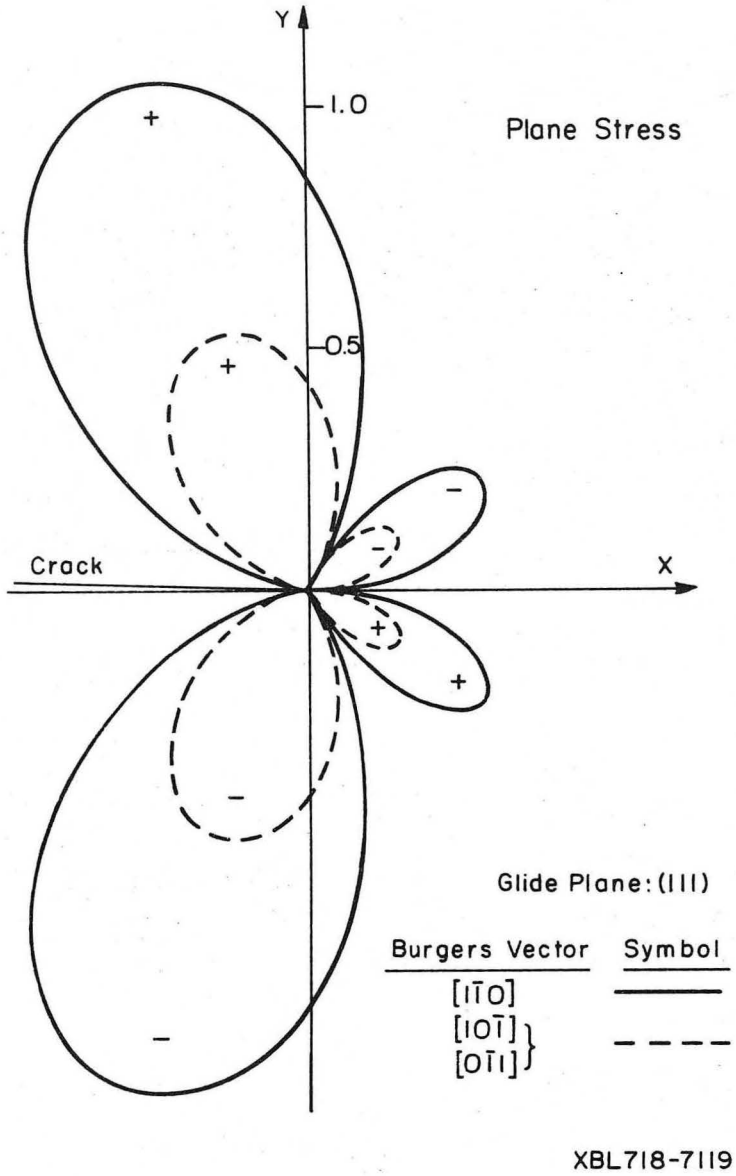
Y
1.0
0.5
Plane Stress
Crack
X
Glide Plane: (111)
Burgers Vector
Symbol
[1$\bar{1}$0]
[10$\bar{1}$]
[0$\bar{1}$1]
XBL718-7119

Fig. 34

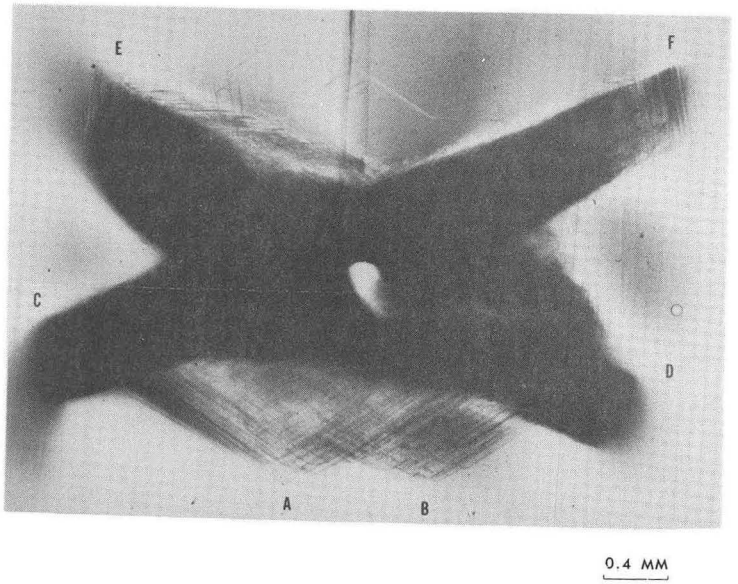

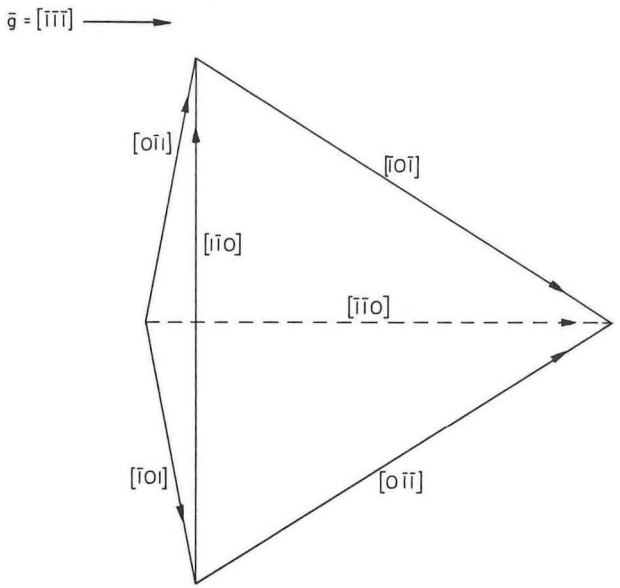

XBB 718-3644

Fig. 35

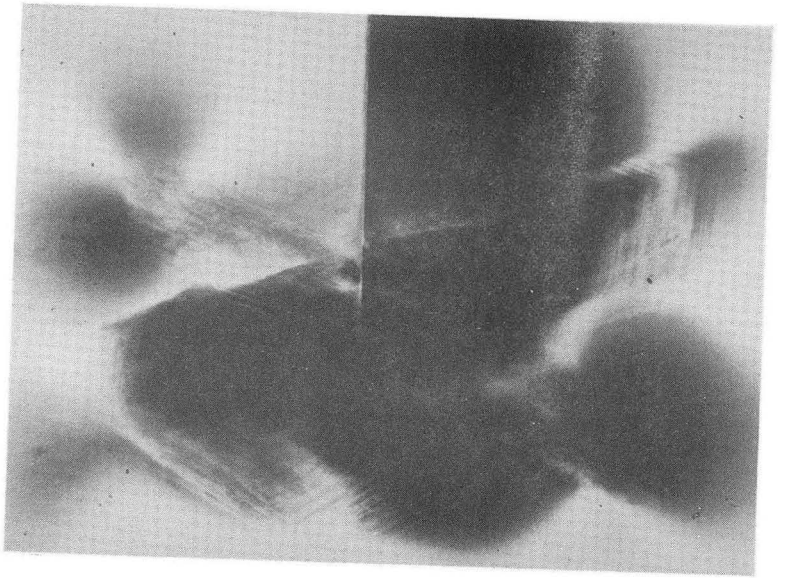

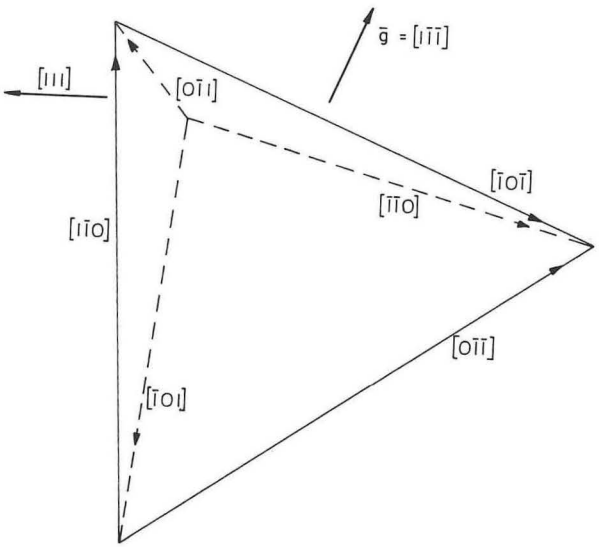

XBB 718-3639

Fig. 36

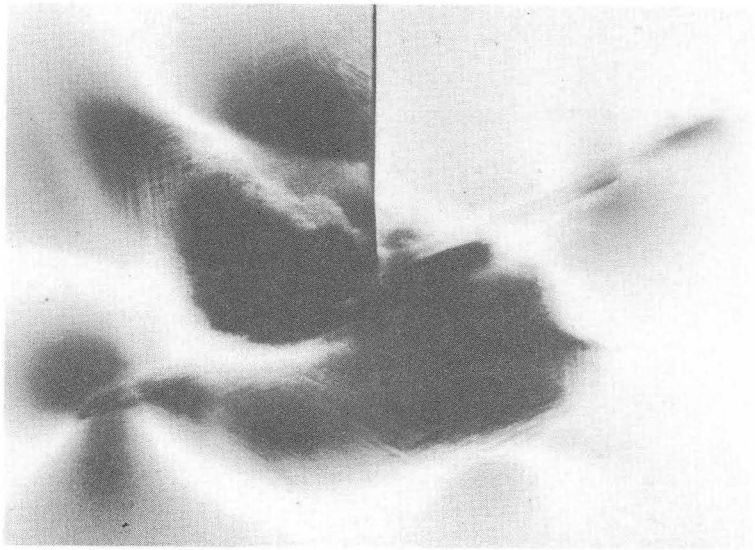

0.4 MM

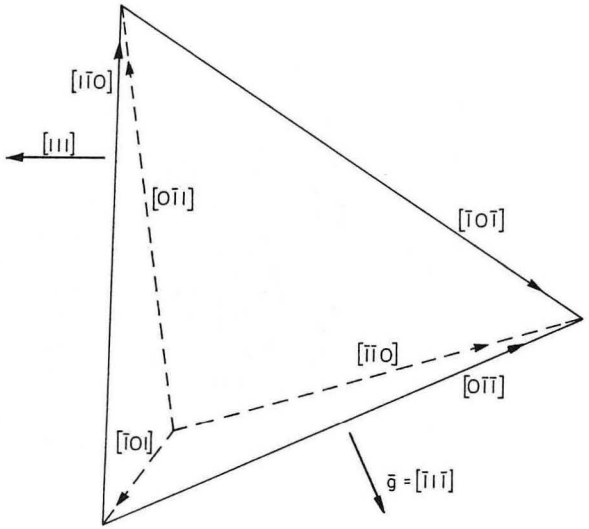

XBB 718-3641

Fig. 37

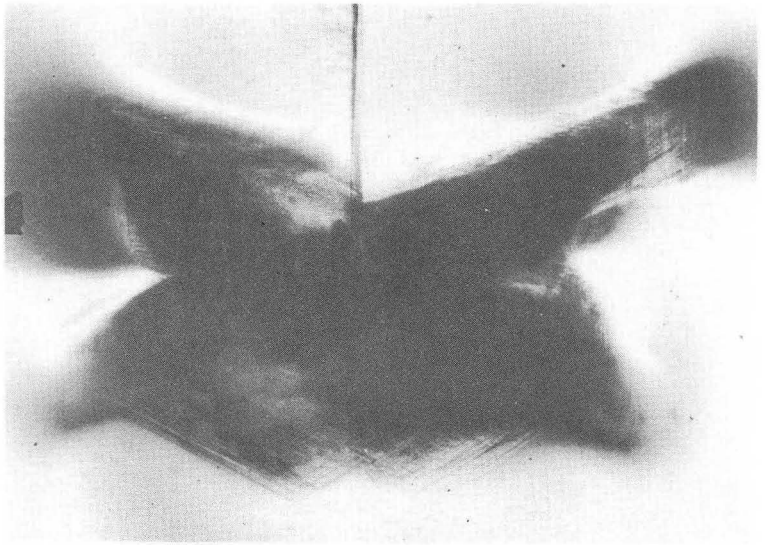

0.4 MM

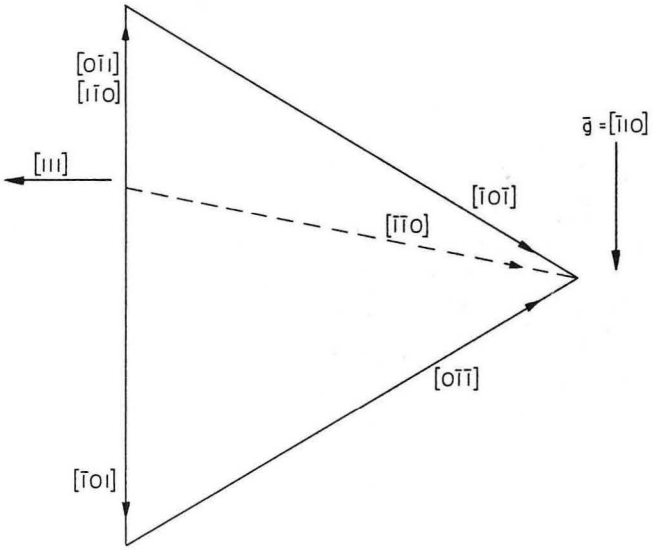

XBB 718-3649

Fig. 38

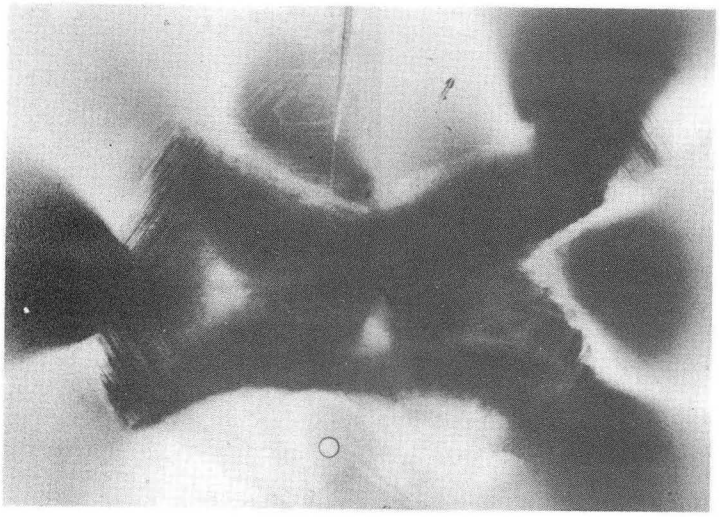

0.4 MM

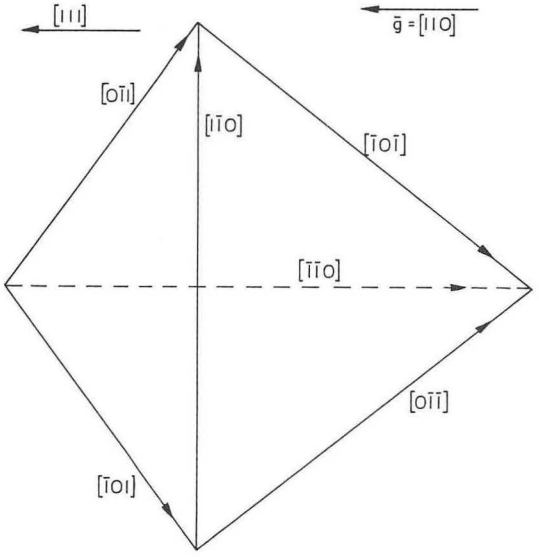

XBB 718-3645

Fig. 39

LEGAL NOTICE

This report was prepared as an account of work sponsored by the United States Government. Neither the United States nor the United States Atomic Energy Commission, nor any of their employees, nor any of their contractors, subcontractors, or their employees, makes any warranty, express or implied, or assumes any legal liability or responsibility for the accuracy, completeness or usefulness of any information, apparatus, product or process disclosed, or represents that its use would not infringe privately owned rights.

TECHNICAL INFORMATION DIVISION
LAWRENCE BERKELEY LABORATORY
UNIVERSITY OF CALIFORNIA
BERKELEY, CALIFORNIA 94720